Quarterly Journal of the Royal Meteorological Society *Q. J. R. Meteorol. Soc.* (2013) DOI:10.1002/qj.2250

Atmospheric response to sea-surface temperature in the eastern equatorial Atlantic at quasi-biweekly time-scales

Gaëlle de Coëtlogon,[a]* Marion Leduc-Leballeur,[a] Rémi Meynadier,[a] Sophie Bastin,[a] Moussa Diakhaté,[b] Laurence Eymard,[c] Hervé Giordani,[d] Serge Janicot[c] and Alban Lazar[c]
[a] *Laboratoire Atmosphère, Milieux, et Observations Spatiales (LATMOS), Paris, France*
[b] *Laboratoire Physique de l'Atmosphère et de l'Océan (LPAO-SF), Dakar, Sénégal*
[c] *Laboratoire d'Océanographie et Climat, Expérimentations et approches Numériques (LOCEAN), Paris, France*
[d] *Centre National de Recherches Météorologiques, Groupe d'études de l'Atmosphère Météorologique (CNRM-GAME), Toulouse, France*

*Correspondence to: G. de Coëtlogon, Laboratoire Atmosphère, Milieux, et Observations Spatiales (LATMOS), Paris, France.
E-mail: gdc@latmos.ipsl.fr

The surface-wind response to sea-surface temperature (SST) and SST meridional gradient is investigated in the Gulf of Guinea by using daily observations and re-analyses in the 2000–2009 decade, with a focus on boreal spring and summer months (May to August), where quasi-biweekly fluctuations in the position of the northern front of the equatorial cold tongue induce quasi-biweekly equatorial SST anomalies. Following a large-scale wind acceleration (deceleration), an equatorial SST cold (warm) anomaly is created within a few days. In order to explain the local atmospheric response to this SST anomaly, the two following mechanisms are invoked: first, a colder (warmer) ocean decreases (increases) the vertical stability in the marine atmospheric boundary layer, which favours a weaker (stronger) surface wind; and second, a negative (positive) anomaly of SST meridional gradient induces a positive (negative) anomaly of the sea-level-pressure meridional gradient, which decelerates (accelerates) the surface wind. The first mechanism has an immediate effect in the equatorial belt between 1°S and 1°N (and to a lesser extent between 3°S and 1°S), whereas the second takes 1 or 2 days to adjust and damps anomalous southeasterlies up to 800 hPa in the low troposphere between 7°S and 1°N, through reversed anomalies of meridional SST and pressure gradient. This negative feedback leads to weaker (stronger) winds in the southeastern tropical Atlantic, which forces the opposite phase of the oscillation within about 1 week. Around the Equator, where the amplitude of the oscillation is found to be maximal, both mechanisms combine to maximize the wind response to the front fluctuations. Between the Equator and the coast, a low-level secondary atmospheric circulation takes control of the surface-wind acceleration or deceleration around 3°N, which reduces the influence of the SST-front fluctuations.

Key Words: air-sea interaction; intraseasonal variability; eastern tropical Atlantic; quasi-biweekly oscillation; SST front; Atlantic cold tongue

Received 30 November 2012; Revised 13 August 2013; Accepted 17 August 2013; Published online in Wiley Online Library

1. Introduction

In the Gulf of Guinea, the surface-wind pattern is dominated by southeasterlies south of the Equator (or Trade Winds), and southerlies between the Equator and the coast. This is shown in Figure 1, with the 2000–2009 mean surface wind, as seen by the Quick Scatterometer (QuikSCAT) in May to June (top) and July to August (bottom). This pattern remains quite the same for the rest of the year, albeit with globally weaker winds (not shown). The winds are driven mainly northward by sea-level pressure (SLP) gradients, from the high-pressure centre in the South Atlantic (the Santa Helena anticyclone) toward the Saharan heat low in West Africa. The meridional SLP gradient increases considerably from April to July because of the northward migration of the solar maximum, which warms up the continent much faster than the ocean (Hastenrath, 1991).

A consequence of this northward migration is a general strengthening of subtropical Trade Winds in the southern Tropics, responsible for an intensification of the coastal oceanic upwellings and inducing a strong sea-surface temperature (SST) cooling in the so-called 'cold tongue' region, in the Gulf of Guinea, during boreal spring and summer (Figure 1). The cold tongue is particularly marked by the presence of a strong meridional SST front on its northern edge, along or slightly north of the

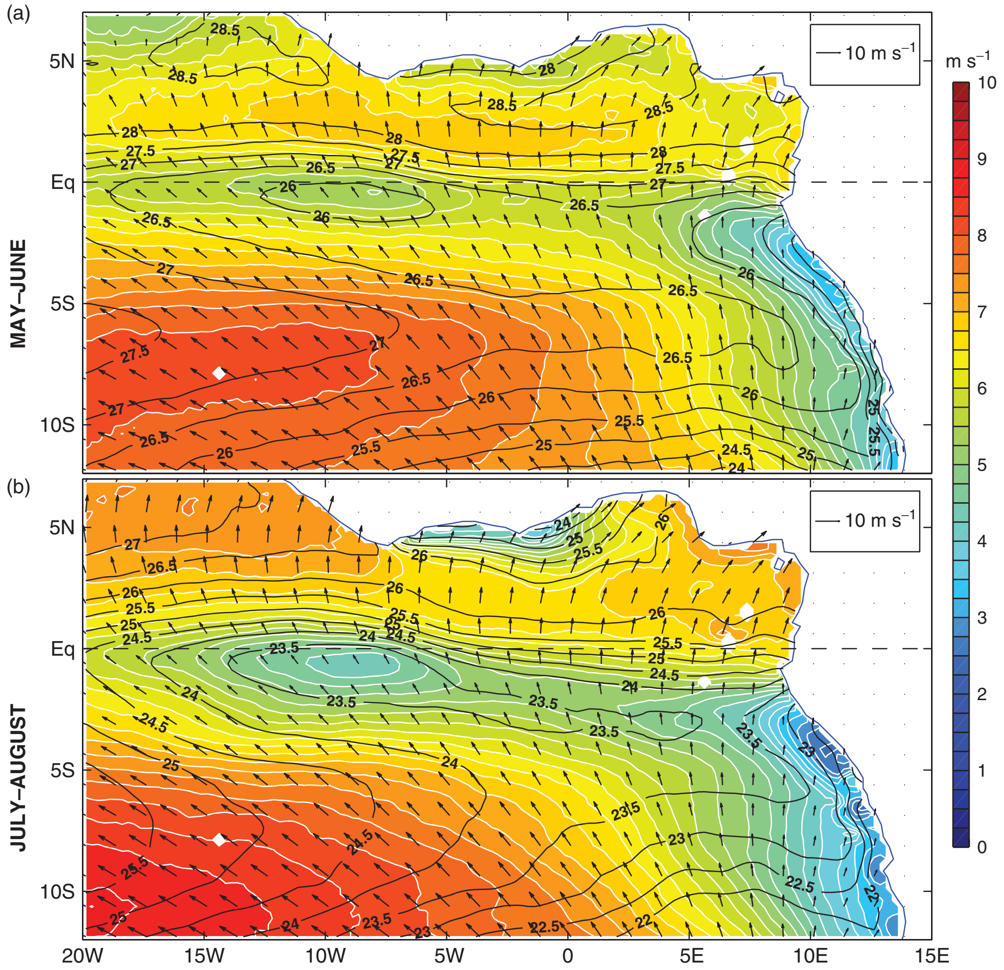

Figure 1. QuikSCAT surface wind (arrows, magnitude in shading) and Reynolds SST (black contours, intervals of 0.5 °C) in May to June (a) and July to August (b), 2000–2009. For clarity, only 1 on 5 × 5 arrows were plotted. This figure is available in colour online at wileyonlinelibrary.com/journal/qj

Equator (Weingartner and Weisberg, 1991). The seasonal cooling of the cold tongue was shown to be driven mainly by the wind-stress increase, enhanced surface-heat fluxes (mainly evaporation) and vertical oceanic entrainment and mixing (Peter *et al.*, 2006; Caniaux *et al.*, 2011; Giordani and Caniaux, 2011; Jouanno *et al.*, 2011; Wade *et al.*, 2011; Giordani *et al.*, 2013).

However, the mean wind decelerates strongly when passing over the cold tongue (Figure 1). According to many previous works, intense SST gradients in coastal and frontal oceanic areas strongly influence turbulent fluxes and modify the circulation in the marine atmospheric boundary layer (or the MABL, see Giordani and Planton, 2000; Bourras *et al.*, 2004; Small *et al.*, 2005; Giordani and Caniaux, 2011; Leduc-Leballeur *et al.*, 2011). This has potential strong effects on the atmospheric circulation and precipitation patterns, because it appears that the convergence of surface winds is generally a cause rather than a consequence of the deep convection (Back and Bretherton, 2009). Two main – and complementary – mechanisms for this oceanic influence on surface winds have been identified in previous studies. First, a cooler SST tends to stabilize the atmospheric column and decreases the vertical momentum flux, decoupling the weaker surface wind from higher stronger wind; and conversely, a warm SST increases the turbulent mixing in the MABL, which increases the surface wind (Sweet *et al.*, 1981; Hayes *et al.*, 1989; Wallace *et al.*, 1989; Xie, 2004). Because of this mechanism (hereafter ‘SW’, as in Sweet *et al.*, 1981), regions with a very sharp SST front are very sensitive to the coupling between SST and surface winds (Xie, 2004; Small *et al.*, 2005). Leduc-Leballeur *et al.* (2011) investigated the mechanisms of this air–sea coupling in 2006 in the Gulf of Guinea, using *in situ* data collected during the 2006 Etude de la circulation océanique et du climat dans le Golfe de Guinée (EGEE) campaign, completed by satellite, and the European Centre for Medium-range Weather Forecasts (ECMWF) operational analyses covering the same period: they showed that the atmospheric surface signal is indeed closely connected to the turbulent MABL dynamics in this region. Second, Lindzen and Nigam (1987) suggested that meridional SST gradients generate anomalous winds through the hydrostatic effect of SST on the SLP. The SST cooling in the eastern Atlantic equatorial band tends to raise the overlying SLP through turbulent surface-heat fluxes, which results in an equatorial decrease of the meridional SLP gradient. As a result, the wind slows down when entering the cold tongue area, and accelerates when it gets out. This mechanism will be referred to hereafter as ‘LN’ (for ‘Lindzen and Nigam’).

Both mechanisms can explain why the patterns of SST and surface-wind magnitude are spatially very much correlated north of 5°S (Figure 1). In general, the SW and LN mechanisms combine to partly control the surface wind by generating secondary circulations in regions marked by intense fronts (Giordani *et al.*, 1998; Samelson *et al.*, 2006; O’Neill *et al.*, 2010a, 2010b). They are difficult to observe at intraseasonal time-scales, because of a strong synoptic noise and nonlinearities. However, their influence on the atmosphere had been well identified from several observational studies (Chelton *et al.*, 2001, 2007; Chelton and Xie, 2010; de Coëtlogon *et al.*, 2010; Leduc-Leballeur *et al.*, 2013).

As can be expected from this tight and complex SST–surface-wind coupling, their seasonal evolution is marked by very large intraseasonal fluctuations in the Gulf of Guinea. De Coëtlogon *et al.* (2010) found a statistical signature of a negative feedback between the observed SST and surface-wind anomalies, around the mean position of the northern front of the cold tongue, in boreal spring and summer. They suggested the following mechanism: the wind strengthening (weakening) leads to a cold (warm) SST anomaly within about 5 days; then, this SST cold (warm) anomaly in turn slows down (strengthens) the surface wind within 2–3 days. Interestingly, the delay of the responses (5–6 days + 2–3 days), completing half a cycle of an oscillation, leads to a full periodicity of about 2 weeks (14–18 days); and indeed, a corresponding periodicity was found to be very robust in the Equator east of 10°W, in the spectrum of both fields. These delays in SST and surface-wind responses were confirmed in Leduc-Leballeur *et al.* (2013); however, the latter focused their study on the downstream (toward the Guinean coast) atmospheric and rainfall responses to the equatorial SST fluctuations. The time-scale of SST fluctuations could be linked as well with tropical instability waves, which are known to result from the barotropic instability of the shear between the equatorial undercurrent and the south equatorial current at this time of the year, but they seem to contribute poorly to the mixed-layer heat budget (Jochum *et al.*, 2004) and are completely controlled by surface-wind fluctuations east of 10°W (Athie and Marin, 2009), where the present study investigates.

All this emphasizes the interest in exploring how much the two mechanisms (SW or LN) drive the atmospheric response to the SST fluctuation, and their involvement in the low tropospheric circulation in the eastern tropical Atlantic. The present work studies these issues through statistical analysis of SST, wind and pressure fluctuations. Although both mechanisms are probably strongly linked to each other, we propose here to make a conceptual distinction between the two by measuring their time and space lags to the SST signal. Previous studies have indeed shown that the near-surface atmospheric mixed layer (associated with SW) reacts in a few hours to a SST modification, whereas the remaining boundary layer (LN) takes 1 or 2 days to adjust (Leduc-Leballeur *et al.*, 2011). The oceanic response to the wind forcing is not discussed here, but we suggest that delays in these coupled responses between surface wind and SST could raise a quasi-biweekly variability, which is very strong in this region.

In addition to satellite observations, which document surface parameters (SST and wind) with very good accuracy, two recent sets of re-analysis have been used: the European Re-analysis (ERA) Interim (ERAI) from the ECMWF, and the Climate Forecast System Re-analysis (CFSR) from the National Centers for Environmental Predictions (NCEP), enabling the study of atmospheric response in the low troposphere. The period of focus will be May to August, because this is the period when the quasi-biweekly equatorial oscillation in the northern front of the cold tongue is the strongest. The data and their processing are first described (sections 2–4). Second, the statistical signature of the SST–surface-wind interaction is compared between observations and re-analyses (section 5). Then, the agreement of this signature with the SW and LN mechanisms is investigated in CFSR and ERAI surface wind and pressure (section 6), and in the low troposphere (section 7). A short discussion (section 8) and a summary (section 9) are then presented.

2. Data

2.1. *Observations*

Surface-wind vectors were provided by the QuikSCAT (Quick Scatterometer) satellite (Liu *et al.*, 2000), available as 3 day running means on a 0.25° × 0.25° grid between 2000 and 2009. A two-dimensional cubic-spline interpolation first filled the gaps due to the clouds for each available day, and then a linear temporal interpolation at each grid point completed the missing days (only amounting to about 15 for the whole decade). QuikScat data are produced by Remote Sensing Systems and sponsored by the NASA Ocean Vector Winds Science Team. Data are available at www.remss.com

The high-resolution SST product developed using optimum interpolation, the Advanced Very High Resolution Radiometer (AVHRR) infrared satellite SST data and *in situ* data from ships and buoys (Reynolds *et al.*, 2007) were retrieved from the NOAA NCDC website, with a spatial grid resolution of 0.25° and a temporal resolution of 1 day.

In addition, the daily averaged TRMM 3B42 product on a 0.25° × 0.25° grid was used. It mixes satellite measurements from microwave sensors and infrared (IR) geostationary instruments with data from ground radars (Huffman *et al.*, 2007), which guarantees the best possible quality for precipitation data. It was retrieved from the website trmm.gsfc.nasa.gov

2.2. *Re-analyses*

Two re-analysis datasets were used: the ERAI from the ECMWF (Dee *et al.*, 2011) and the CFSR (Saha *et al.*, 2010) from the NCEP. One of the distinctive CFSR characteristics is the coupling of atmosphere and ocean models, which provides an advantage for the air–sea interaction study.

The re-analyses data are available on a 0.75° × 0.75° horizontal grid for the ERAI and 0.5° × 0.5° for the CFSR, with vertical atmospheric profiles retrieved on 27 levels from 1000 to 100 hPa for both. For this study, the daily mean of the six-hourly parameters is used over the decade 2000–2009.

3. Comparison of mean SST and surface winds in observations and re-analyses

In the eastern tropical Atlantic, the May–June (MJ) period corresponds to a transition between the oceanic phase of the West African Monsoon and its coastal phase (see Thorncroft *et al.*, 2011; Leduc-Leballeur *et al.*, 2013, or Nguyen *et al.*, 2011 for details), which precedes the seasonal northward migration (or 'monsoon jump') by 2–4 weeks. Figure 1(a) shows a maximum band of surface-wind velocity standing between the Equator and the Guinean coast. In July–August (JA), this band of stronger winds is still present, together with stronger subtropical Trade Winds further south, but surface winds weaken considerably when entering the cold tongue area: in its core, between 5 and 10°W, a wind of 5.5 m s^{-1} is found for a SST of 26 °C in MJ; it weakens down to 4 m s^{-1} for a SST of 23.5 °C in JA.

The SST and 10 m wind differences between the two re-analyses and the observations were plotted for May–August (MJJA) 2000–2009 (Figure 2). The wind is in general too weak in the ERAI, where the band of wind maximum north of the Equator is strongly underestimated (by more than 1 m s^{-1}, see Figure 2(b)). In the CFSR, the wind is too weak along the Guinean coast, but is slightly too strong further south, especially along the Equator west of 3°W (Figure 2(a)) and in the coastal region south of 5°S. The equatorial wind bias (of $<$0.75 m s^{-1}) is collocated with a small SST cold bias (of $<$0.2 °C). However, these are common flaws seen in models and re-analyses: because being the centres of strong air–sea interactions, regions of strong horizontal gradients, or frontal areas, are very difficult to represent realistically. On average, the re-analyses for the ERAI and CFSR have a good degree of confidence for performing statistical analyses, with $<$0.2 °C of difference in their SST and 2 m s^{-1} (1 m s^{-1} only in the CFSR) in their wind, compared with the observations (except in coastal upwellings).

4. Intraseasonal variability *versus* seasonal evolution

The amplitude of the seasonal cycle in the eastern tropical Atlantic is very important, but intraseasonal fluctuations are also very large; a good way to compare both time-scales in real time is to have a look at the time–latitude diagram of SST and wind averaged between 10°W and 0 (where the SST equatorial front is the strongest), as for the year 2007 plotted in Figure 3. This particular year was chosen because it exhibited very regular oscillations of the SST front (seen in Figure 3(c) along the Equator), but quasi-biweekly oscillations were also found in other years (not shown). The front position, its intensity and oscillations in latitude are

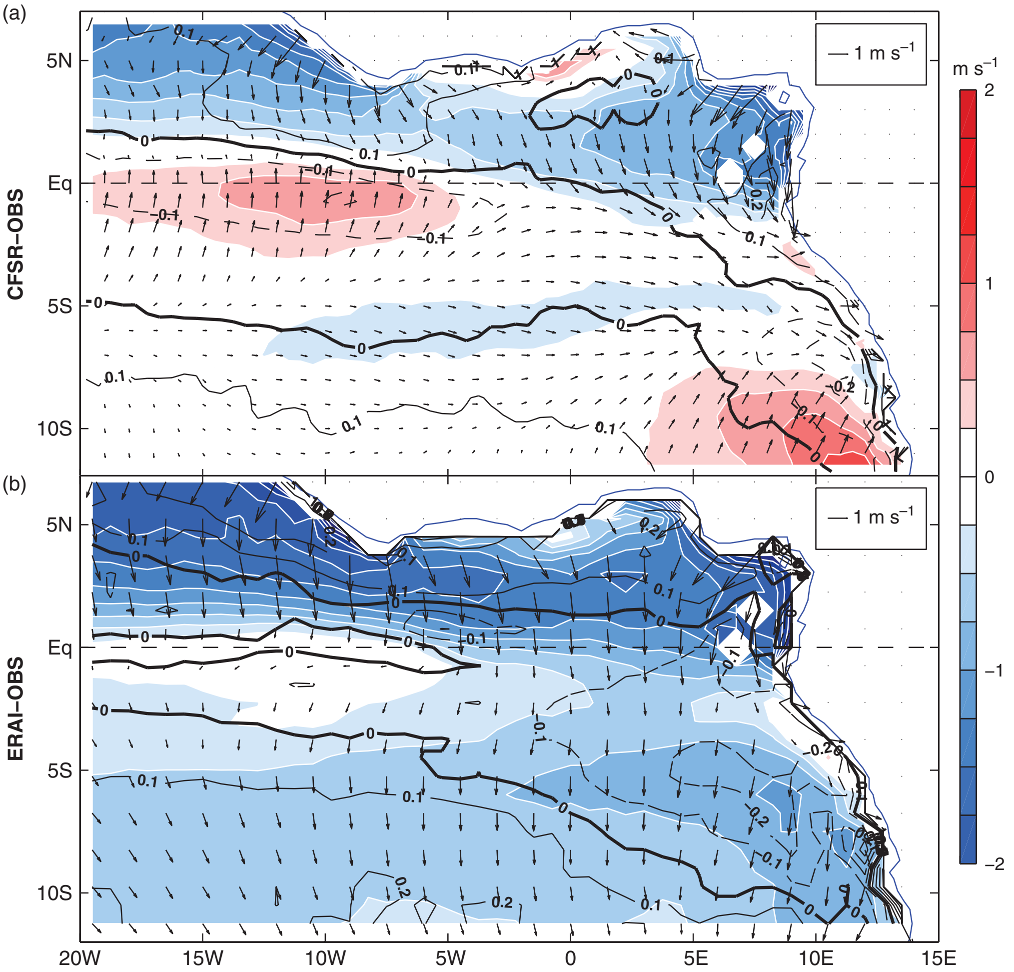

Figure 2. Differences between the re-analyses and observations (OBS), May to August, 2000–2009: for 10 m wind (magnitude in shading, and bias direction in arrows; for clarity, only one in nine arrows were plotted for the CFSR, and one in four for the ERAI) and SST (black contours, intervals of 0.1 °C, solid for positive, dashed for negative): (a) the CFSR and (b) the ERAI. The SST and wind observations were first interpolated on the re-analyses grids, and then the mean of the difference computed. This figure is available in colour online at wileyonlinelibrary.com/journal/qj

better seen in the meridional SST gradient (or more precisely the variation of SST for 1° of latitude, Figure 3(b)). The seasonal appearance and disappearance of the front appears to coincide with the establishment of the late spring and summer wind acceleration between the Equator and the coast (Figure 3(a)), through a relatively large negative meridional pressure gradient there (Figure 3(c)). South of the Equator, in contrast, a weaker pressure gradient (Figure 3(c) with a value corresponding to -10 Pa latitude-degree^{-1} contoured in white, as it is a local minimum in the cold tongue region) combined with the SW effect over colder waters tends to slow down the overlying wind.

In addition to this clear seasonal evolution, the SST and wind patterns exhibit some very marked intraseasonal fluctuations, such as the quasi-biweekly oscillations in the northern front of the cold tongue investigated in this study. Note that these oscillations were shown to partly control the wind strength between the Equator and the Guinean coast, which largely influences the Guinean coastal rainfall and seems to actively contribute to its seasonal onset (Leduc-Leballeur *et al.*, 2013). The amplitude of the front oscillations is about 1 or 2° in latitude around the Equator, and increases during July to August, as the oceanic mixed layer is shoaling and the thermocline approaches closer to the surface, which amplifies the oceanic response to the surface-wind forcing (Giordani and Caniaux, 2011).

Intraseasonal SST fluctuations were obtained by removing seasonal time-scales with a high-pass Lanczos filter (cut-off at 90 days), thereby exhibiting clear quasi-biweekly anomalies (see Figure 3(d)). In the 0.5°S to 1°N band, which corresponds to the mean position of the front, intraseasonal SST anomalies are the largest and exhibit a standard deviation of about 0.5° in MJJA: there is a cold anomaly when the front is located anomalously north, or a warm one when the front is further south. As in de Coëtlogon *et al.*, (2010), a 'northern cold tongue index' (NCTI) was built by averaging the high-passed filtered SST data in this area (more precisely: between 8°W and 4°W, and 0.5°S to 1°N, which frames intraseasonal SST anomalies of maximum variance). All regressions presented below are performed onto this NCTI, because it characterizes the SST-front variability in an accurate way.

The spatial distribution of quasi-biweekly time-scales for the observed SST and surface wind is shown in Figure 4. Beforehand, the MJJA time series were band-passed between 10 and 20 days, their root mean square (RMS) computed and divided by the RMS of intraseasonal anomalies (<90 days): this produces an estimation of the 10–20 day variance fraction among the total intraseasonal variance. The square of this value is plotted in Figure 4, in order to obtain percentage values. It appears very clearly that this 'quasi-biweekly' part is maximal along the northern front of the cold tongue (45% in the wind, 40% in the SST). As the ocean reacts slower than the atmosphere, it was expected to obtain less variance at shorter time-scales, but this value is nonetheless much larger in the equatorial band than anywhere else in the South Atlantic. The northern front of the cold tongue is therefore the place where quasi-biweekly oscillations are the largest.

5. Lagged linear regression of surface parameters

Lagged linear regressions of different surface fields were performed onto the NCTI as defined immediately above. For reasons of simplicity, they are presented here as time (lag) *versus* latitude diagrams, after having averaged the parameters between 10°W

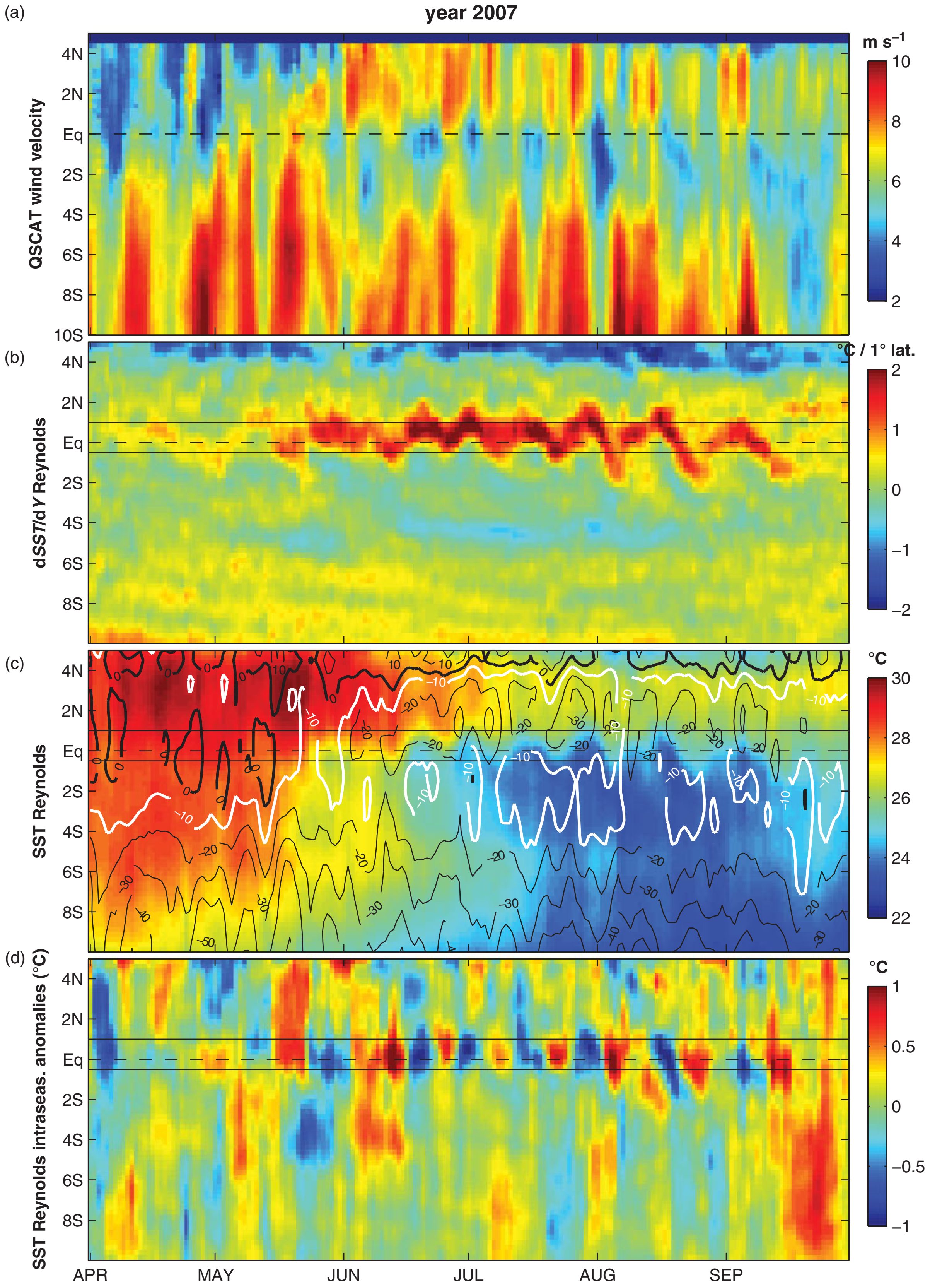

Figure 3. Time–latitude diagrams from April to September 2007, 10°W–0: (a) QuikSCAT wind magnitude, (b) meridional gradient of Reynolds SST, (c) Reynolds SST (shading) and meridional gradient of CFSR SLP (black contours, zero line in heavy, intervals of 10 Pa per latitude degree, dashed lines for positive, solid for negative, white contour for value −10 Pa per latitude degree) and (d) intraseasonal SST Reynolds anomalies. Black lines at 1°N and 0.5°S frame the SST averaged to build the northern cold tongue index (NCTI; see text for details). For clarity, a running spatial filter over 3° latitude grid points (i.e. 1.5° latitude) and three time points (i.e. 3 days) was applied to the meridional gradient of the SLP. This figure is available in colour online at wileyonlinelibrary.com/journal/qj

and 0°E, and high-pass filtered them (with the same Lanczos filter as the NCTI, with a cut-off at 90 days). Note that extending the area eastward to 5°E does not change the results shown here, but slightly decreases their robustness. For the QuikSCAT wind, the three following components were considered independently: the surface-wind magnitude (computed before the high-pass filtering) and its zonal and its meridional components. A particular period of the year in the 2000–2009 decade was selected: MJ, JA, or MJJA. Then, the regression patterns of anomalies were computed as the lagged correlation with the NCTI, weighted by the standard deviation of the field (in order to obtain amplitudes in physical units, such as °C for the SST regression, or m s^{-1}

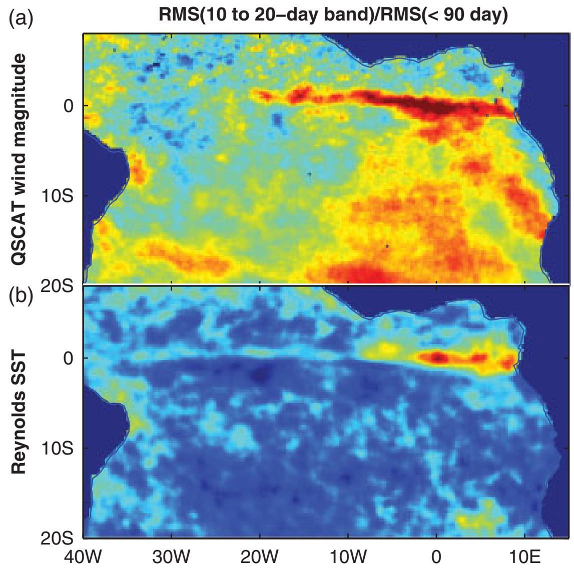

Figure 4. Percentage of 10–20 day band-passed RMS *versus* 90 day high-passed RMS in MJJA, 2000–2009, for QSCAT wind-stress magnitude (a) and Reynolds SST (b) time series. This figure is available in colour online at wileyonlinelibrary.com/journal/qj

for the wind fields). All the following regression patterns have been chosen to be represented with a *minus* sign, therefore corresponding to the correlation patterns with a *cold* anomaly of SST in the NCTI; but as linear regression is used here, opposite patterns are of course just as significant. In all that follows, 'significant correlations' mean 'above the 90% significant threshold' (i.e. null hypothesis rejected with a risk of 10% to be incorrect). The 90% significant correlation is 0.08 when considering 10 years of 123 days, divided by a persistence of about 3 days, i.e. 410 degrees of freedom. In short, these regressions show the patterns of anomalies significantly correlated to a SST cooling of about 0.5 °C in the region of the front, a few days before (negative lags), at the same time (lag 0) and after (positive lags) the cold anomaly is maximal: for example, 'lag -5' for a wind regression means that the NCTI is correlated with the wind 5 days before.

Figure 5(a) shows the lagged linear regression patterns of QuikSCAT wind anomalies (magnitude in colours) and Reynolds SST (black contours) on the NCTI for MJJA. At lag 0, around the Equator, a cold SST anomaly of about 0.5 °C corresponds to a weaker wind anomaly of up to 0.4 m s^{-1}. At negative lags, i.e. before the SST anomaly is the coldest, a stronger wind anomaly is found upstream of the Equator. This stronger wind 'pushes' the front northward (it actually intensifies the SST gradient further north, with half being accounted for by increasing the advection of colder waters northward, and half by the vertical entrainment and diffusion, see de Coëtlogon *et al.*, 2010), which results in the developing cold SST anomaly. From lag 2 onwards, the surface wind responds to the SST cooling by significantly weakening in the equatorial band. This atmospheric response seems to be fast, with a maximal anomaly at lags 1 or 2. Further south, a weak (southward) but significant wind anomaly is also found during the following lags, as far as 10°S from lags 2–5. About 1 week after the cold SST anomaly is maximal, opposite patterns are observed in the equatorial SST and surface-wind anomalies (albeit much damped), with a warmer SST coinciding with stronger overlying winds, signifying a quasi-biweekly periodicity. The latter could result from a negative air–sea feedback south of 2°N: a stronger surface wind cools down the SST, which weakens the surface wind, which warms up the SST, and so on, as was suggested by de Coëtlogon *et al.* (2010). North of 2°N, a northward wind anomaly is sustained until lag 3, and even amplified with a maximum at lag 2. This signature of a positive feedback in the wind strength combines with a clear change in its zonal orientation, turning from northwestward at lag 5 to northeastward at lag 2 (Figure 5(a)). This is in agreement with de Coëtlogon *et al.* (2010), who obtained similar results with the Tropical Rainfall Measuring Mission's Microwave Imager (TMI) SST.

Two identical NCTIs were computed with the SST in both re-analyses, the ERAI as well as CFSR, and similar regressions performed on their 10 m wind and SST fields. The resulting anomalous wind and SST patterns are in broad agreement with observations, i.e. a large-scale wind burst precedes an equatorial SST cooling by 4–5 days, which in turn slows down the overlying wind south of 2°N within 1 or 2 days, while sustaining it north of 2°N (Figure 5, (b) for the CFSR and (c) for the ERAI). Amplitudes of the atmospheric responses are considerably weaker, however, especially in the ERAI: with comparable initial SST anomalies of about −0.5 °C and observations giving an equatorial wind decrease of about 0.4 m s^{-1} as a response (at lags 1 or 2), the 10 m wind weakens by less than 0.2 m s^{-1} in the ERAI and slightly more than 0.3 m s^{-1} in the CFSR. Therefore, the surface-wind response to the SST seems to be better represented in the CFSR than in the ERAI, but is still underestimated compared with the observations. These results are in good agreement with Maloney and Chelton (2006), who found that a response of the wind to the SST in their models becomes weaker as the model grid-spacing increases, given that the resolution is better in the CFSR (0.5°) than in the ERAI (0.75°). Maloney and Chelton (2006) also mentioned the vertical resolution (similar in both re-analyses) and deficiencies in the parametrization of boundary layer physics to explain this poor response, even when the spatial resolution is very high. Another reason for the better response in the CFSR than in the ERAI, however, could be attributed to the air–sea coupling, which

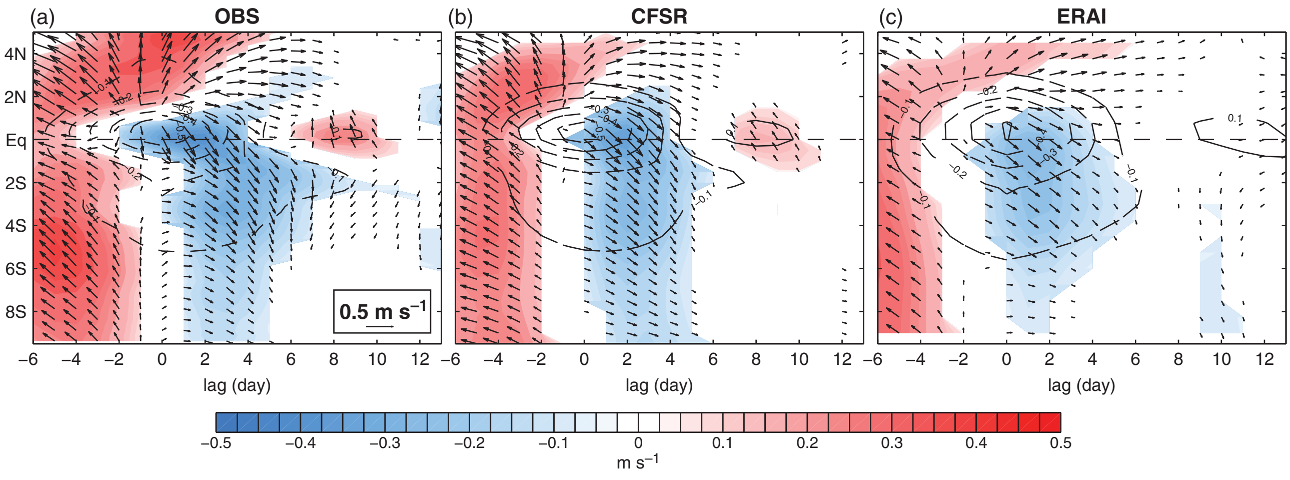

Figure 5. Time–latitude diagrams of linear regressions on the NCTIs, 10°W–0, May to August, 2000–2009: anomalies of surface wind (arrows for direction, magnitude in shading, m s^{-1}) and SST (black contours, intervals of 0.1 K, dashed for negative) from observations (a) QuikSCAT and Reynolds,: (b) the CFSR and (c) the ERAI. Only significant values are shown. This figure is available in colour online at wileyonlinelibrary.com/journal/qj

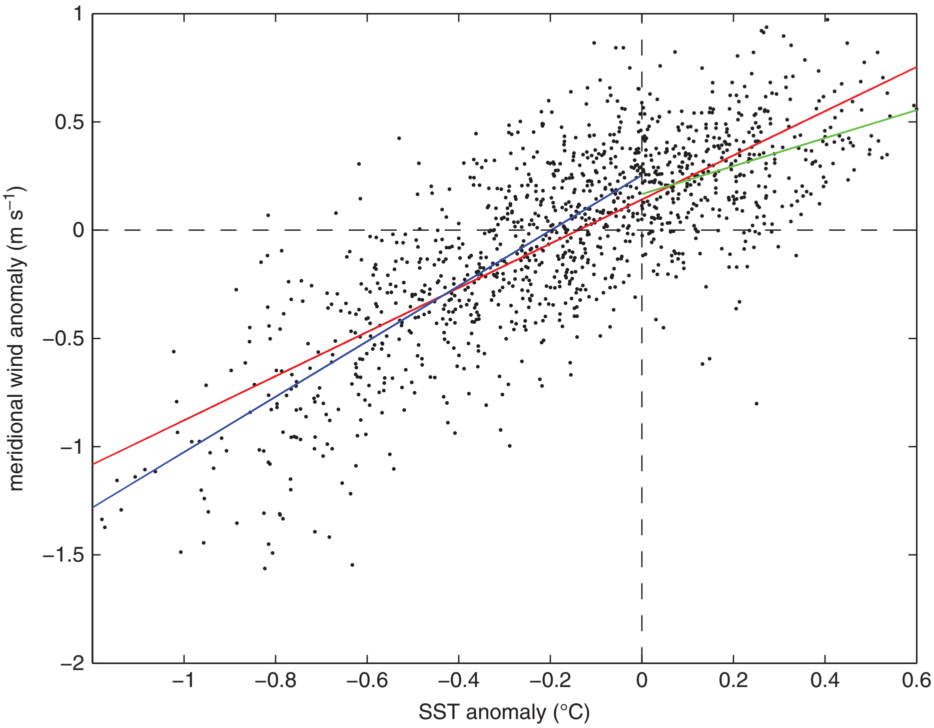

Figure 6. Linear regression between high-pass spatially filtered Reynolds SST and QuikSCAT surface wind in the front region (10°W–0/0.5°S to 1°N), May to August, 2000–2009 (red line; one dot per day). Blue and green are regression lines for respectively negative and positive SST anomalies. This figure is available in colour online at wileyonlinelibrary.com/journal/qj

is active in the CFSR, together with an assimilation of surface observations, SST and surface wind (Saha *et al.*, 2010).

6. Response of the atmospheric surface

The statistical signature of the atmospheric response can be interpreted by invoking the two physical processes described in section 1.

6.1. *The SW effect (vertical momentum flux in the MABL)*

The fast adjustment of the MABL dynamics to the cold anomaly, even though small, can be seen in Figure 5(a): at negative lags, the perfect match between the pattern of the cooling SST (in black contours) with the decreasing overlying wind (in colour) in the equatorial band, even before the cold SST anomaly has fully developed, can only mean that this mechanism takes place immediately. This is also seen with the secondary maximum at lags 8–10, when the SST is warmer and the wind stronger.

The SW mechanism seems to be particularly active along the Equator, where SST anomalies are the largest. The surface-wind anomalies were averaged in the NCTI box (8°W- to 4°W/0.5°S to 1°N), and their correlation with the NCTI computed: it is 0.43 for MJJA, which is a highly significant value. However, a higher correlation (almost 0.48) is reached when the SST leads the wind by 2 days, which can be speculated from Figure 5(c) around the Equator at lag 2. In order to emphasize the local (small-scale SST features and immediate SW) response *versus* the large-scale response (SST gradients and 1–2 days delayed LN), a high-pass spatial filtering of SST and wind velocity was performed by running windows of 1000 km in longitude and 500 km in latitude, following Chelton *et al.* (2001), before computing the SST and wind index in the NCTI box: an even larger correlation (0.77) between them is obtained, with a maximum at lag 0. The corresponding scatter plot for MJJA, 2000–2009, is shown in Figure 6: it clearly produces a slope of about 1, i.e. about 0.5 m s^{-1} stronger (weaker) wind anomaly for a 0.5 °C warmer (colder) SST anomaly. Moreover, the relationship seems to be quasi-linear between the SST and wind anomalies, with only a slight difference of slopes when considering negative or positive SST anomalies.

In order to quantify the wind response to the SST at the other latitudes, the correlation between these spatially high-passed filtered wind speed and SST (averaged between 10°W and 0°E) anomalies was computed at each available grid latitude, in observations as well as in re-analyses (Figure 7). In MJ, wind speed and SST are highly correlated between 3°S and 1°N, with values slightly larger in observations (between 0.5 and 0.8, with a clear maximum at the Equator) and the CFSR (0.6–0.7) than in the ERAI (0.45–0.65). It is interesting to note that the correlations dramatically reduce north of 1°N in observations, but not so much in the CFSR. In JA, values are comparable to the MJ correlations in observations (except between 5°S and 3°S), whereas they strongly decrease in both re-analyses (where they are generally <0.5). Obviously, re-analyses do not reproduce the surface atmospheric response to the SST very well in JA, therefore only results based on the months of May and June will be shown hereafter.

Figure 8 shows the linear regressions corresponding to the correlations in Figure 7: each large dot or star corresponds to a specific latitude in Figure 7, and indicates in Figure 8 the typical amplitude of the wind anomalies (RMS) and their correlated SST anomalies (i.e. the SST – wind correlation, times the RMS of the wind anomalies). The wind responses exceed 0.4 m s^{-1} of stronger (or weaker) wind for a SST warmer (or cooler) by about 0.4 °C in the observations (blue dots and stars) around the Equator, and about 0.15 m s^{-1} for 0.15 °C around 3°S. It confirms a tendency for the wind to respond linearly to a SST fluctuation according to the SW mechanism between 3°S and 1°N, with a maximal correlation clearly located in the equatorial band (inside 1°S to 1°N), and a general response factor of about 1 m s^{-1} per 1 °C. This is in good agreement with previous observations and estimations (such as in Chelton *et al.*, 2001). The wind response is much smaller in re-analyses, and is nonlinear (especially in the ERAI), with only 0.5 to slightly more than 0.75 m s^{-1} of wind response per 1 °C of SST anomaly in the CFSR, and 0.25 to nearly 1 m s^{-1} in the ERAI.

6.2. *The LN effect (the SLP gradient)*

Lagged regressions were performed onto the NCTI with CFSR and ERAI intraseasonal SLP and SST anomalies in MJ (Figure 9,

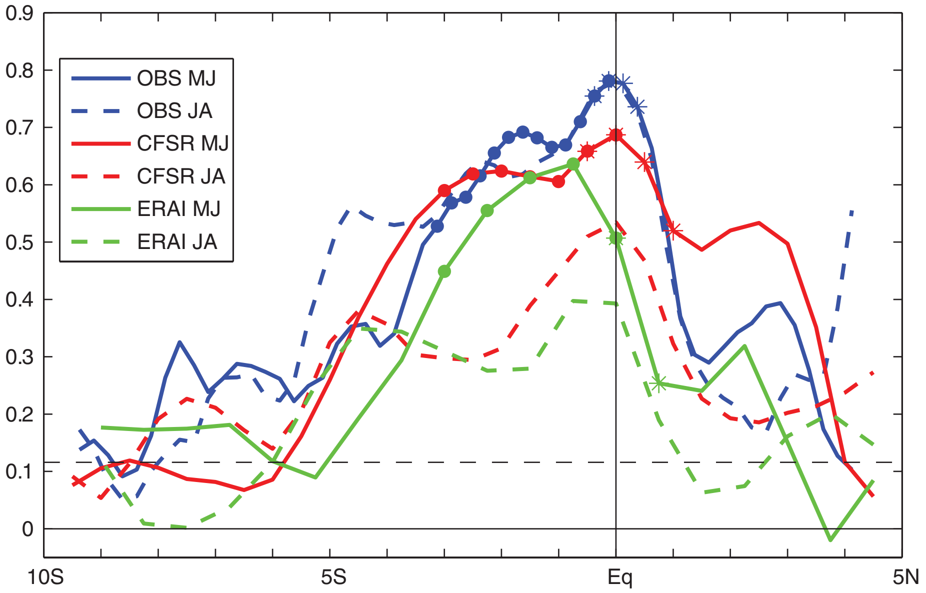

Figure 7. Correlation between intraseasonal SST and wind anomalies, averaged 10°W–0, in observations (blue), the CFSR (red) and the ERAI (green), for MJ (solid) and JA (dashed), 2000–2009. Horizontal black dashed line gives the 90% significant correlation level with a persistance of 3 days taken into account in the time series. This figure is available in colour online at wileyonlinelibrary.com/journal/qj

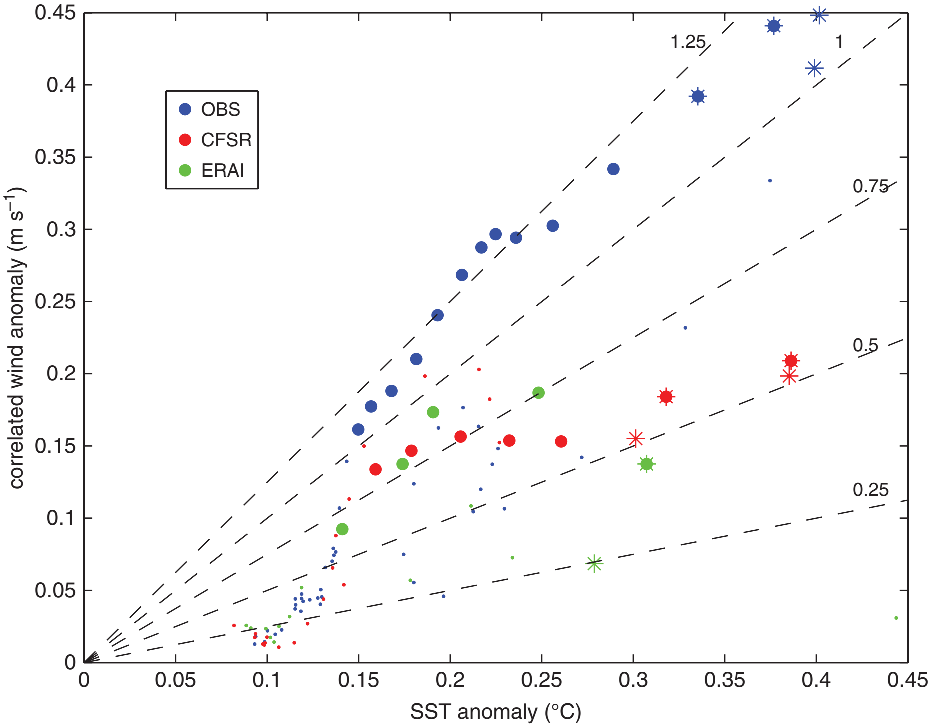

Figure 8. The RMS (SST) *versus* correlation (SST, wind) times RMS (wind), in the observations (blue), the CFSR (red) and the ERAI (green), for MJ, 2000–2009 (small dots). Large dots and stars mark some particular latitudes, which are indicated in Figure 6. Black dashed lines show the five different slopes from 0.25 to 1.25. Spatially high-passed filtered SST and wind velocity anomalies were used here. This figure is available in colour online at wileyonlinelibrary.com/journal/qj

top row). They slightly differ from the amplitudes obtained with MJJA anomalies (as shown in Figure 4): at lag 1 or 2, the equatorial SST anomaly is smaller in the ERAI (0.35 instead of 0.5), while equatorial wind anomalies are considerably larger in both re-analyses (0.8 instead of 0.5 m s^{-1} in the CFSR, and slightly less than 0.5 instead of 0.2 m s^{-1} in the ERAI; see Figure 9, top row), which confirms that surface winds are more sensitive to the SST fluctuations in the MJ than in MJJA or JA in re-analyses.

Both re-analyses show an anomalous high pressure developing over and after the cold SST maximum, with a maximum pressure anomaly found at lags 1 or 2 (Figure 9, top). Its amplitude is rather weak, being of 10–15 Pa only, but it is nonetheless significant. In the CFSR, this positive SLP anomaly is probably created by the cold SST anomaly through a negative latent-heat-flux anomaly of about −15 W m^{-2} (Figure 9, bottom left): as the SST is cooler, and the wind weaker than normal over the cold SST anomaly, there is less evaporation. This latent-heat-flux feedback is much weaker in the ERAI, with a small anomaly in surface solar radiation (Figure 9, bottom right). A modest positive solar radiation anomaly, centred rather north of the SST anomaly, is also found in the CFSR, but around 3°N, which corresponds to a precipitation increase in the two previous lags (not shown), and matches well with the observations (Leduc-Leballeur *et al.*, 2013). Amplitudes of other sensible-heat-flux and long-wave-radiation flux anomalies do not exceed 3 or 4 W m^{-2} in both re-analyses. The SLP anomaly in the ERAI therefore must be created by the atmosphere above, and/or by the constraints of the re-analysis scheme toward radiosoundings and satellite measurements.

The high SLP anomaly is found to be maximal between 1°N and 2°N, i.e. slightly north of the cold SST anomaly: in the

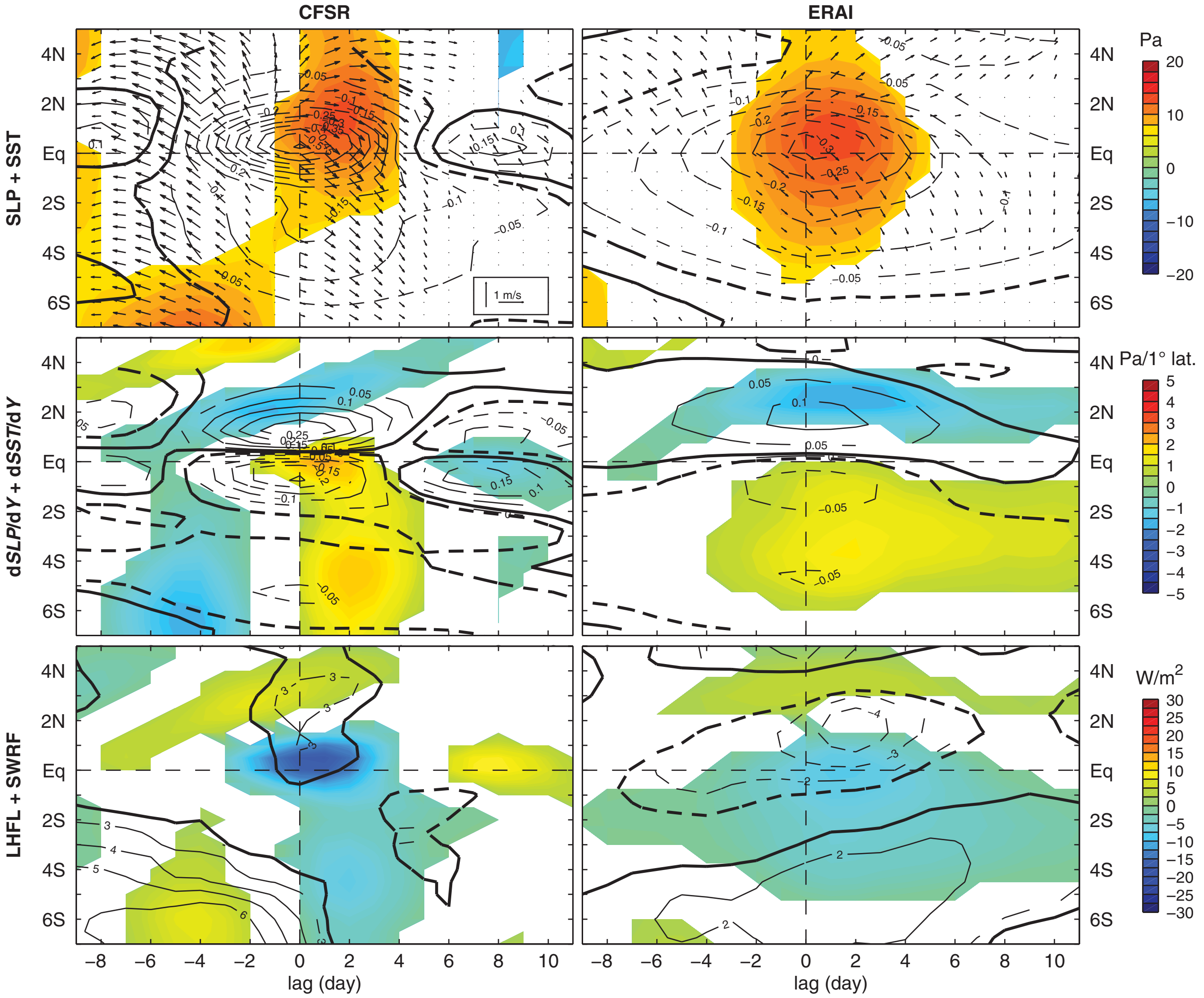

Figure 9. Lagged linear regression on the NCTI in the CFSR (left) and the ERAI (right), 10°W–0, MJ 2000–2009. (Top) Anomalies of the SLP (colours) and SST (black contours, intervals of 0.05 K). Arrows stand for 10 m surface-wind anomalies as in Figure 4 (right). (Middle) Anomalies of d*SLP*/d*Y* (colours) and d*SST*/d*Y* (black contours, intervals of 0.05 K per latitude degree). (Bottom) Anomalies of surface latent-heat flux (colours) and short-wave radiation (black contours). Only significant values are shown. Fluxes are positive upward. Heavy black lines contour the 90% significant correlation level. Black lines are solid for positive, dashed for negative. This figure is available in colour online at wileyonlinelibrary.com/journal/qj

time it takes for the SLP to respond to the cold SST anomaly (1–2 days), the SLP anomaly may be transported northward by southerlies. A similar delay was observed by Small *et al.* (2005) in the eastern equatorial Pacific, and by Spall (2007) in an idealized numerical simulation of a front. However, the SLP signal is certainly less dispersed when the wind is weaker, which should give more weight on the ‘weak wind days’ when computing the correlation and the mean SLP anomaly position: **t**he observed displacement is about 1° north, while a stream of 5 m s^{-1} during 1 day should theoritically displace an anomaly of about 4°. This positive SLP anomaly nonetheless explains the change in surface-wind direction between the Equator and the coast: wind anomalies are rather westward at negative lags, and progressively turn eastward at positive lags, deflected by the growing SLP anomaly (Figure 9, top), because at these latitudes (i.e. north of 2°N) the Coriolis effect is not negligible.

As for the negative lags, i.e. before the cold SST anomaly is maximal, no particularly interesting SLP signal is observed: there is only an expected reinforced negative meridional gradient (barely seen in the ERAI for this area), corresponding to a higher than normal Santa Helena anticyclone, which precedes the SST equatorial cold anomaly through increased surface southerlies (de Coëtlogon *et al.*, 2010; Caniaux *et al.*, 2011; Leduc-Leballeur *et al.*, 2011). South of 3°S in both re-analyses, negative wind anomalies are found significant between lags 1 and 6, and even as far as 8°S in the CFSR, where no significant SLP signal can be seen to sustain them (Figure 9, top). If the meridional gradient of the SLP (hereafter d*SLP*/d*Y*) is considered instead of the SLP itself, however, a significant positive anomaly is found with a maximum at lag 2, at around 5°S in the CFSR (Figure 9, middle left) and 3°S in the ERAI (middle right). Its value is very small, but nonetheless can explain the weaker wind anomaly further north: with the geostrophic relationship $w = \frac{1}{\rho|f|}|\nabla p|$ (w is the wind strength anomaly, $\rho$the air density taken as 1.2 kg m^{-3}, f the Coriolis parameter $2\Omega\sin(\text{latitude})$ and $|\nabla p|$ the magnitude of the pressure gradient anomaly, mostly equal to $|dSLP/dY|$ in this region), an anomaly of about 2 Pa per degree of latitude at 4°S (such as found in Figure 9, middle row) is sufficient to drive a wind anomaly of about 1.5 m s^{-1}, way larger than the 0.3–0.8 m s^{-1} found in both re-analyses (Figure 9, top row). Amplitudes of d*SLP*/d*Y* anomalies, albeit small, are therefore large enough to explain the observed wind anomalies through the geostrophy south of the Equator. Note that the differences can be attributed to the friction at the surface and to the mixing with the free tropospheric circulation, that both explain why the meridional SLP gradient can drive meridional, and not only zonal, winds (Matsuno, 1966; Stevens, 2002; Small *et al.*, 2005; Back and Bretherton, 2009). In particular, the friction becomes progressively comparable, and then much larger, than the geostrophic balance in the equations of motion when getting close to the Equator. A positive anomaly of 2–3 Paper latitude degree just south of the Equator (around 0.5°S) is also found in the CFSR, while being weaker in the ERAI: it probably drives a part of the southern wind anomaly there, in addition to the SW mechanism. It is impossible to tell how much

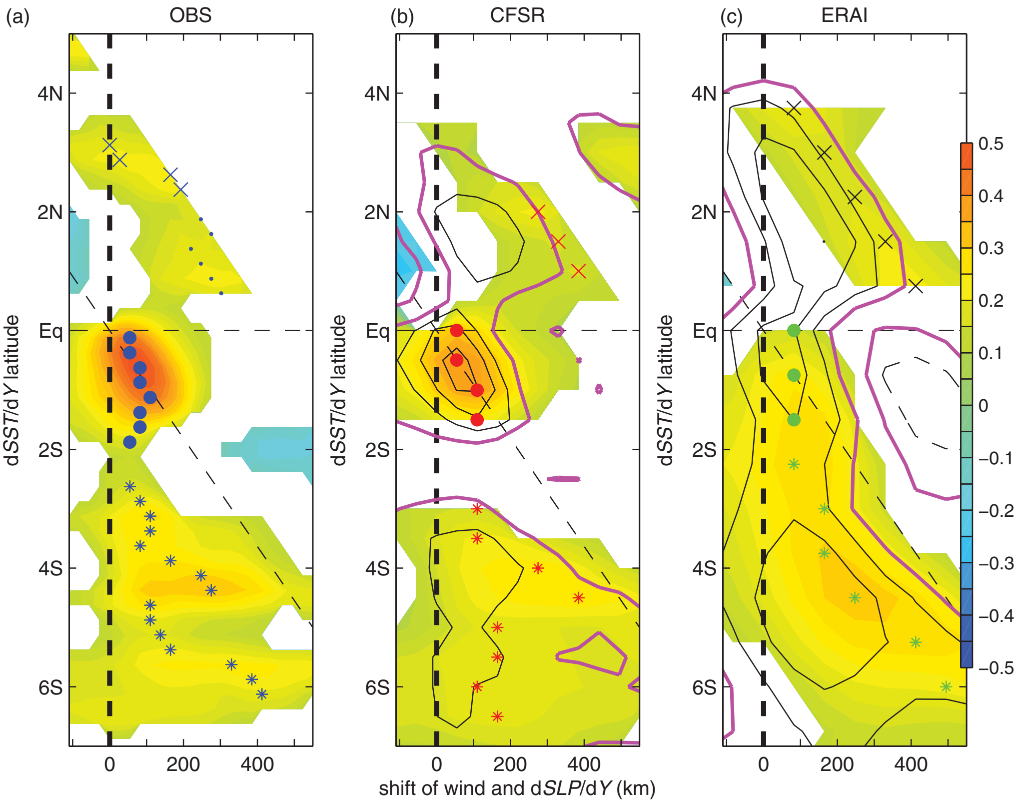

Figure 10. Correlation between intraseasonal anomalies of dSST/dY and surface-wind strength (colours) or dSLP/dY (black and pink contours), MJ, 2000–2009, averaged in the 10°W–0 band, in (a) the observations, (b) the CFSR and (c) the ERAI, when the wind lags by 0–3 days (the maximal correlation is retained). The x-axis corresponds to the wind (or dSLP/dY) shift in latitude (positive if northward, negative if southward), in relation with the dSST/dY latitude (indicated by y-axis). Markers (dots, crosses and stars) indicate the maximal correlation at each latitude. Light dashed lines show Equator positions, as seen by the SST gradient (horizontal) or by the wind response (vertical). Heavy dashed line follows the correlation between dSST/dY and local (non-shifted) wind. When the SLP is available (the CFSR and the ERAI), the pink contour corresponds to the first significant correlation (i.e. 0.11), followed by black contours every 0.1 (solid for positive, dashed for negative). This figure is available in colour online at wileyonlinelibrary.com/journal/qj

the two effects contribute to the wind anomaly there, but as the pressure gradient anomaly is maximal at lag 1, it suggests that the LN mechanism would indeed lag the SW effect by 1 or 2 days.

A regression onto the NCTI was performed with SST meridional gradients, or dSST/dY hereafter (Figure 9, middle row). Anomalies of dSST/dY and dSLP/dY are obviously in complete agreement with SST and SLP anomalous patterns in both re-analyses, but they give a complementary view by emphasizing gradient anomalies that are significant, without regard to the amplitude of the anomalies themselves: albeit rather weak, the spatial scale of the latter could indeed be small enough to produce large gradients. Invoking the LN mechanism, in the CFSR, slightly south of the Equator (around 0.5°S), the large negative dSST/dY anomaly explains the positive dSLP/dY anomaly seen at lag 1 or 2 and discussed above (Figure 9, middle left). Further south, around 5°S (i.e. in the progressively appearing southern flank of the cold tongue), a secondary maximal (negative) dSST/dY anomaly matches well the secondary maximal (positive) dSLP/dY anomaly discussed above, albeit slightly further north (advected northward by the mean atmospheric flow). This picture is quite similar in the ERAI, although the cold SST anomaly is smaller (0.35 °C instead of 0.5 °C) and more widespread in the meridional direction, which leads to much smaller amplitudes of dSST/dY anomalies and without any maximum just south of the Equator.

South of the Equator, wind anomalies therefore seem to be controlled by dSLP/dY anomalies that can be explained by dSST/dY anomalies through the LN mechanism. This is confirmed by computing the correlation between dSST/dY and wind speed, or dSST/dY and dSLP/dY anomalies, at each latitude, taking into account the fact that the wind speed or dSLP/dY may take 1 or 2 days to fully respond to dSST/dY, with a northward shift (due to mean southerlies advection): Figure 10 shows these correlations when the wind or dSLP/dY lag dSST/dY by 1 or 2 days (the maximum value between the two lags was kept), and the x-axis indicates the north–south shift of the wind or dSLP/dY. In the observations, the dSST/dY correlation with the wind speed is found to be maximal around 0.5°S, with a wind response shifted north by 50–100 km (Figure 10(a)): this maximum corresponds to the southern side of the northern front of the cold tongue, where the dSST/dY variance – and then its potential impact on dSLP/dY or wind – is clearly maximal. On the northern side of the front, the maximal correlation is smaller (around 0.2) and shifted further north. A relative low correlation is found at 3°S, but it increases again between 3 and 6°S (around the southern front of the cold tongue), with a northward shift of 100–300 km.

All this confirms the significant influence of dSST/dY on the wind speed in the whole Gulf of Guinea, as far as 7°S. For comparison, in the CFSR the dSST/dY–wind speed-anomaly correlation pattern is broadly similar, but with lower values (0.3 instead of 0.5 at 0.5°S) north of 7°S, and in the ERAI, a good correlation is found south of the Equator but without any maximum around 0.5°S, such as in the observations or the CFSR. Eventually, the correlations between dSST/dY and dSLP/dY in the CFSR (Figure 10(b)) and the ERAI (right) prove that this influence of dSST/dY on the wind is made through pressure gradients, since very large correlations are found at about the same latitudes and northward shifts (albeit weaker) than the largest dSST/dY–wind speed correlations.

By retrieving the maximal shifted wind response at each dSST/dY grid latitudes, as indicated by the different markers in Figure 10, a regression similar to that in Figure 8 was performed in order to quantify the dSST/dY influence on the surface wind speed (Figure 11). The largest linear response was found in observations, and amounts to roughly 4–5 between the Equator and 2°S (big blue dots), and further north around 3°N (blue crosses), meaning that a dSST/dY of about 0.1 °C per latitude degree drives 0.4–0.5 m s^{-1} of wind there. It is not linear south of 3°S (blue stars), but with roughly similar – or higher – coefficients,

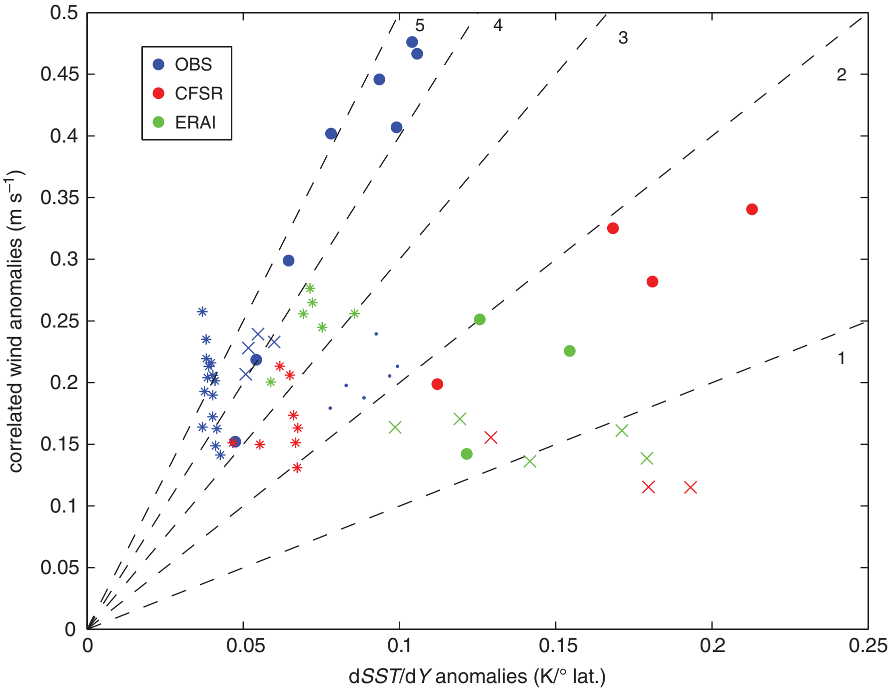

Figure 11. The RMS ($\mathrm{d}SST/\mathrm{d}Y$) *versus* correlation ($\mathrm{d}SST/\mathrm{d}Y$, wind) times RMS (wind), in the observations (blue), the CFSR (red) and the ERAI (green), for intraseasonal anomalies of $\mathrm{d}SST/\mathrm{d}Y$ and wind, averaged 10W–0, in MJ, 2000–2009. For each latitude, maximal values of correlation when the wind is shifted north are kept, with the different markers indicating latitude ranges, as in Figure 8. Black dashed lines show the five different slopes from 1 to 5. This figure is available in colour online at wileyonlinelibrary.com/journal/qj

although $\mathrm{d}SST/\mathrm{d}Y$ and wind anomalies have smaller amplitudes. On another hand, in the CFSR (red) and the ERAI (green), the response coefficients are only 1–2 between the Equator and 2°S (big dots), and even smaller north of the Equator (crosses). Re-analyses therefore strongly underestimate the wind response to the meridional gradients of SST in the whole Gulf of Guinea, especially north of 2°S. Note that the wind response to $\mathrm{d}SST/\mathrm{d}Y$ in JA was found to be quite similar to the MJ results in the observations, but significantly smaller in both re-analyses.

It is quite surprising to find a relatively low response of the wind between the Equator and 2°N in observations (small blue dots in Figures 10 and 11), because the most intense values of $\mathrm{d}SST/\mathrm{d}Y$ in boreal spring and summer (like seen in Figure 3, and corresponding to the northern front of the cold tongue) are located exactly there. This suggests that, in spite of an obvious seasonal influence (the wind acceleration between the Equator and the coast clearly coincides with the front installment in 2007 – see Figure 3, and in other 2000–2009 years as well – not shown), the influence of the front on surface winds could be more complex than a simple direct LN effect north of the Equator. Moreover, the SLP gradient anomaly on the northern side of the growing cold SST anomaly exhibits a maximum at lags -2 or −1 in the CFSR (Figure 9, middle left), i.e. before the positive SST gradient anomaly (which would create the SLP gradient anomaly through the LN effect) is fully developed. This is the same for the wind acceleration between the Equator and the coast in observations and the CFSR, which precedes the maximal SST anomaly by 1 or 2 days (Figure 5). Finally, Figure 4 shows a weak quasi-biweekly variance between the Equator and the Guinean coast, whereas a large one would have been observed if the front oscillations directly influence the surface wind there. In total this suggests that, in addition to the LN and SW effects in the atmospheric boundary layer, other dynamics must be involved in the wind response to the SST or $\mathrm{d}SST/\mathrm{d}Y$ north of the Equator, such as a secondary circulation in interaction with the Guinean coast.

7. Response of the low troposphere

Different atmospheric fields from the CFSR and the ERAI re-analyses on all available pressure levels from 1000 to 100 hPa were averaged between 10°W and 0. The latitude/altitude averages for MJ and JA are plotted in Figure 12, showing the different components of the wind. The Tropical Easterly Jet is found around 200 hPa both in MJ and JA. The African Easterly Jet is located at 600 hPa, between 6°N and 10°N in MJ and north of 10°N in JA, in agreement with previous studies (Cook, 1999). The westerly monsoon flow is also found below 900 hPa north of 3°N, with a jet located between 6°N and 8°N (Pu and Cook, 2010).

The southward return flow of the shallow meridional circulation is clearly observed in MJ around 700 hPa, in both re-analyses. In JA, it is weaker and located further north in the CFSR, but has almost disappeared in the ERAI. Note that this secondary maximum in the tropospheric meridional wind (the first maximum being at 100–200 hPa, in the upper branch of the Hadley cell) was first found by Trenberth *et al.* (2000) and characterizes regions under monsoonal influences, such as the Indian Ocean. The strongest shallow meridional circulation (SMC) was found in West Africa (Zhang *et al.*, 2008). An important deep convection is also visible at the coast (around 5°N), as well as a low-level recirculation between the Gulf of Guinea and the coast, which appears here as an extension of the SMC: it is the low atmospheric local circulation (LALC) described in Leduc-Leballeur *et al.* (2013, see also Nguyen *et al.*, 2011; Thorncroft *et al.*, 2011), located on average between roughly 8°S and the coast in MJ, but confined between the Equator and the coast during a large-scale southern wind burst.

In JA, after a seasonal transition generally in late May or early June, the LALC is definitely located between the Equator and the coast, with a northward surface wind always stronger there than south of the Equator (Leduc-Leballeur *et al.*, 2013). Precipitation in the re-analyses was compared with the TRMM B42 product, however, although the CFSR and ERAI rainfall profiles match well with observations in MJ (Figure 12(a)), there is a huge discrepancy in their JA profiles (Figure 12(b)). Rain maximum is located 200–400 km too far south, which is a common flaw in numerical models investigating the West African monsoon. In addition, there is a huge secondary maximum of precipitation located at the coast (5°N) in the CFSR, which clearly shows that the coastal deep convection must be exaggerated. One explanation would be that the SMC over the continent is too intense in the CFSR, maybe because of some flaws in the representation of moisture

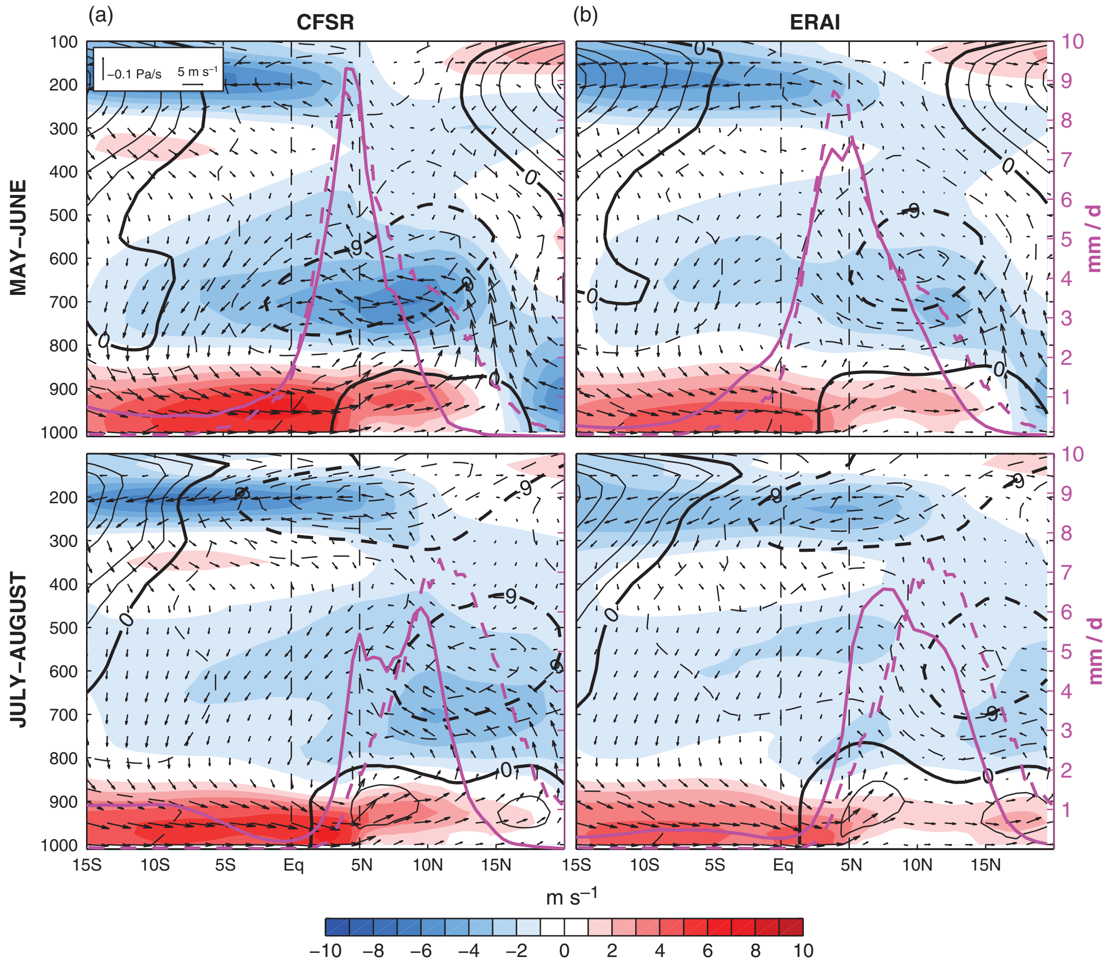

Figure 12. Meridional – vertical circulation in (a) the CFSR and (b) the ERAI, MJ 2000–2009, 10°W–0: meridional and vertical velocities (vectors), meridional velocity (shading, interval contours of 1 m s^{-1}) and zonal velocity (black contours, intervals of 3 m s^{-1}, dashed for negative, plain for positive, heavy for values 0 and −9). Precipitation profiles in re-analyses (plain magenta) and TRMMB42 (dashed magenta), in mm day^{-1}. This figure is available in colour online at wileyonlinelibrary.com/journal/qj

meridional gradients, as in much of the operational analyses and re-analyses investigated in Meynadier *et al.* (2010). On another hand, Thorncroft *et al.* (2011) suggested that the SMC is mostly driven by the contrast between oceanic high pressure and the Saharan heat low, and that a mid-level SMC appears to favour a southern location for the rain band, whereas the low-level monsoonal flux appears at a more northern location: it is plausible that both re-analysis models do not represent this ocean–continent contrast correctly in summer (because of flaws such as in the model vegetation cover). For this reason, further investigations focus on MJ only. In addition, as quite similar results were obtained with the ERAI, results are shown only for CFSR data.

Lagged linear regressions below 500 hPa were performed onto the NCTI in an identical way to that described in the previous section, with meridional and vertical winds (Figure 13, first row), geopotential height (or Z hereafter, second row), Z meridional gradient (dZ/dY hereafter, third row) and zonal wind (last row). Note that a positive (negative) Z anomaly is equivalent to a higher (lower) pressure; a positive (negative) dZ/dY anomaly tends to force a southward (northward) wind close to the Equator; and in the zonal direction, by geostrophy (outside of the 2°S to 2°N band approximately), a positive (negative) dZ/dY anomaly supports eastward (westward) wind anomalies in the Northern Hemisphere, and westward (eastward) in the Southern Hemisphere. In that way it is possible to follow the vertical development of pressure anomalies and pressure gradient anomalies from the surface, in response to the SST and dSST/dY anomalies, and their impact on the wind.

At lag -2, stronger than normal southerlies are observed in the MABL, with anomalies up to 0.5 m s^{-1} (Figure 13, top left). They match a large-scale negative dZ/dY anomaly (bottom left), which exhibits significant values in the whole MABL as far as 3°N, supporting anomalous southeasterlies (third row, left). This pattern, which lasts a few days, is in broad agreement with a stronger than normal South Atlantic anticyclone, which amplifies the (negative) meridional pressure gradient and generates large-scale subtropical subsidence with stronger surface southeasterlies in the Gulf of Guinea (see de Coëtlogon *et al.*, 2010 or Marin *et al.*, 2009). These wind anomalies are smaller in the ERAI (<0.2 m s^{-1}, not shown). Around the coast at 5°N, a column of strong positive dZ/dY anomaly is found (Figure 13, bottom left), together with an increased coastal convergence, as described in Leduc-Leballeur *et al.* (2013). The LALC is then stronger than normal, with a deep subsidence anomaly slightly north of the Equator, and stronger than normal wind in the atmospheric boundary layer around 3°N. This secondary circulation would be maintained by the latent heat release at the coast, leading to a positive feedback during 2–3 days (Leduc-Leballeur *et al.*, 2013).

At lag 3, the anomalous strong coastal deep convection has stopped and the subsidence branch of the LALC has migrated further north. This northward migration has followed the northern side development of the Z anomaly, plotted as a Z 'bubble' rising from the surface at lag 0 where dZ/dY anomalies were maximal (Figure 13, see the green line at lags 0 and 3): dZ/dY exhibits a positive anomaly on its southern side around the Equator, which probably decelerates the southerlies there, and a negative anomaly on its northern side at 2.5°N to 3°N, which would accelerate the southerlies.

South of the Equator, the large-scale negative dZ/dY anomaly at lag -2 becomes positive at lag 3 (Figure 13, bottom row): in agreement with this signal, stronger than normal winds in the MABL become weaker than normal (Figure 13, top row). A similar

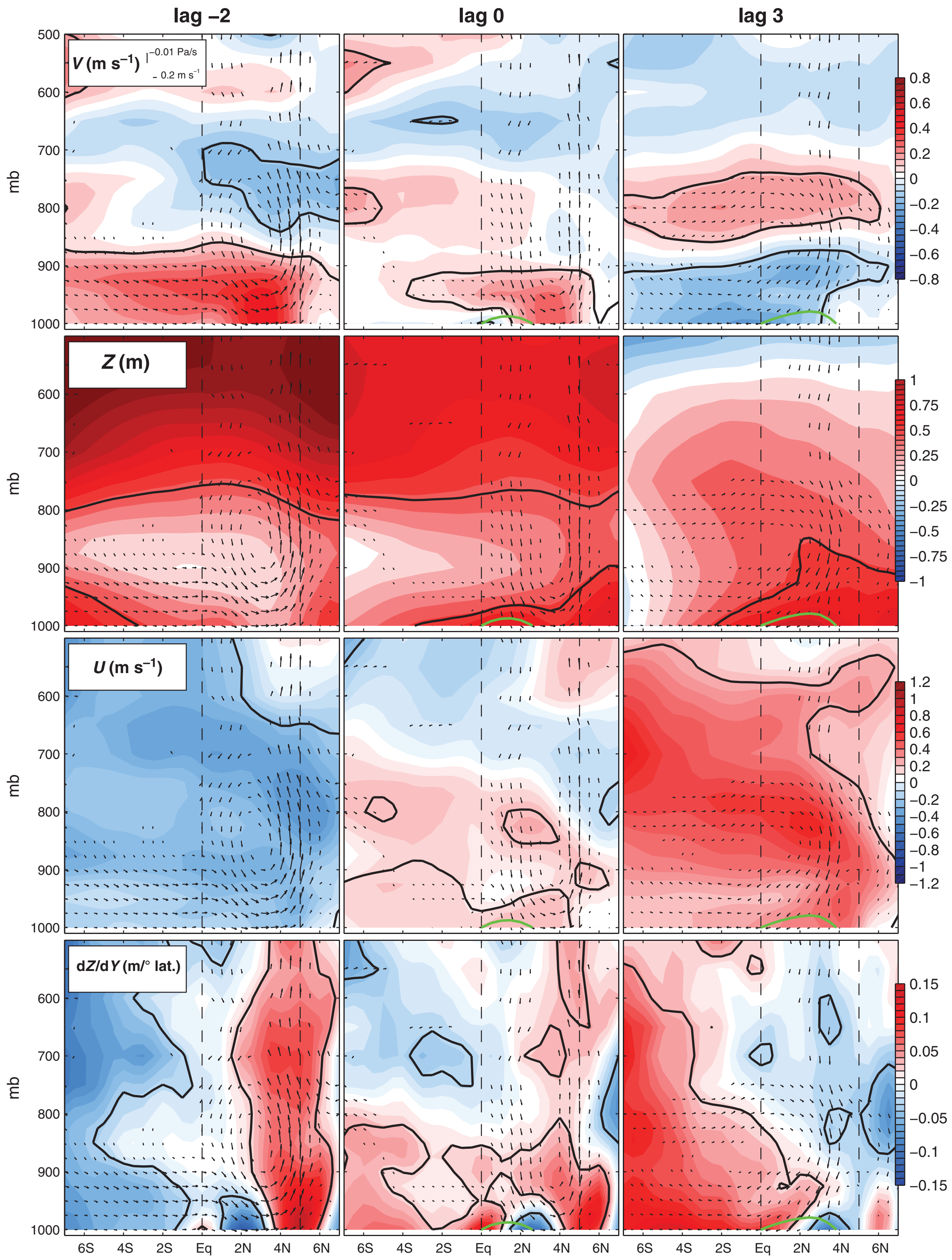

Figure 13. Lagged linear regression on the NCTI, MJ 2000–2009, 10°W–0, in the CFSR: anomalies of vertical meridional circulation (arrows), meridional velocity (top row), Z (second row), zonal velocity (third row), and Z meridional gradient (bottom row). Black lines contour significant anomalies, plain for positive and dashed for negative. Green lines contour a constant Z anomaly starting from maximal dZ/dY anomalies at the surface. Only significant anomalies of vertical or meridional velocity are shown. This figure is available in colour online at wileyonlinelibrary.com/journal/qj

inversion is observed in the low tropospheric zonal wind, with anomalies turning from westward to eastward (Figure 13, third row). The control for this inversion clearly comes from the oceanic surface through the LN mechanism, because the largest (positive) dZ/dY anomalies at lag 0 are found close to the surface around the Equator and at 5°S, where the largest dSST/dY anomalies are (Figure 9, middle). The dZ/dY anomalies have spread upward from the surface at lag 3. This mechanism appears to reverse wind anomalies well above the MABL south of the Equator. In the ERAI, a very similar inversion in dZ/dY and surface-wind anomalies is observed, except that it develops 1 or 2 days sooner than in the CFSR, and seems to extend higher in the low troposphere (not shown). This is an important result, suggesting that the negative feedback between boundary layer winds and meridional SST gradients could actually contribute to the strong quasi-biweekly oscillation observed in the cold tongue region.

8. Discussion

A similar low tropospheric response was found in JA as in MJ, but with slightly smaller amplitudes (not shown), possibly because at this time of the year the continental surface has taken control of the monsoon flux (Thorncroft *et al.*, 2011; Caniaux *et al.*, 2011), limiting the influence of the sea. As the atmospheric large-scale forcing is stronger in JA than in MJ, northward advection and friction at the surface are also larger, which could weaken their response to SLP anomalies as well. In addition, the re-analysis does not represent well the summer monsoon circulation in JA, thereby limiting its reliability.

The dZ/dY signals found in the ERAI were comparable to those in the CFSR (section 7) when considering the low tropospheric parameters, with very similar patterns. In particular, their geopotential height anomalies clearly show the same anomalous pressure 'bubble' rising from the surface around the Equator, with strong dZ/dY anomalies at its edges; and further south, the pattern of reversed dZ/dY anomalies is also very similar. However, the wind-anomaly amplitudes remain smaller in the ERAI, and not very accurate in their timing around lag 0, both in amplitude and spatial accuracy, especially near the surface (not shown).

Section 5 also showed that the ERAI obviously represents less well the intraseasonal air–sea coupling than the CFSR when considering the surface parameters (i.e. SST and wind). The vertical resolution in both re-analysis models (only five points between 1000 and 900 hPa, which broadly represents the MABL) obviously does not allow a precise reproduction of the SW mechanism. But the wind decreases more rapidly at the surface than at the top of the MABL when responding to a NCTI cold signal (see Figure 13, top row, lag 0), in the CFSR as well as the ERAI (not shown), therefore suggesting at least a partial reproduction of the SW mechanism. This creates a divergence in surface-wind anomalies around 1°N and could thus contribute to force the subsiding branch of the LALC over the northern front of the cold tongue (just as the increased convergence at the coast would force its anomalous upward branch).

The signals associated with the LN mechanism were also broadly well represented. The wind responses are too weak in both re-analyses, however, which could indicate some flaws in the parametrizations. As they are particularly weak in the ERAI surface parameters, this could suggest a large sensibility of the surface-wind response to the planetary boundary or surface layer parametrizations, which would be more pertinent in the CFSR.

On the other hand, the better wind response in the CFSR could be due to the active air–sea coupling, which modifies the intradaily SST (the SST Reynolds being daily assimilated in both re-analyses) through the 'free' intradaily surface-heat fluxes: the coupling would act like some form of 'correction' on the wind, improving the heat-flux feedback and the wind reactivity to SST fluctuations. The intradaily coupling frequency has indeed a strong impact on how intraseasonal variability is represented in a model (Masson *et al.*, 2012).

Eventually, when computing fractions of quasi-biweekly variance as in Figure 4, values for the wind were found to be much smaller than for the SST in both re-analyses (not shown), in contrast to the observations. This is probably due to the wind response, which is too weak in the models, and therefore suggests that the air–sea coupling controls a large part of the quasi-biweekly variability in the equatorial Gulf of Guinea. Note, however, that biweekly periodicities are also found to be important in the surrounding eastern subtropical South Atlantic (Figure 4): they can be present in the synoptic perturbations crossing the southern basin; westward-propagating and convective atmospheric Rossby waves could also have an imprint in this biweekly signature (Kikuchi and Wang, 2009). Other factors inherent to the West African Monsoon are also potentially involved in the signals presented here, such as surface latent-heat fluxes and Madden–Julian oscillations (Sobel *et al.*, 2010), easterly waves and fluctuations of the African Easterly Jet (Lafore *et al.*, 2011), atmospheric Kelvin waves (Nguyen and Duvel, 2008), Saharian Heat Low excursions (Lavaysse *et al.*, 2010), or the diurnal cycle with nocturnal jets having large consequences on the inhibition of convection over the continent (Knippertz *et al.*, 2011).

9. Summary and conclusion

Results obtained, along with the observations, clearly suggest that intraseasonal fluctuations of surface winds are strongly controlled by the SST or its meridional gradient in the Gulf of Guinea, as far as 7°S: through a combination of both LN and SW mechanisms between 1°N and 3°S, and through the LN mechanism alone further south. The SW mechanism seems to be especially important in the equatorial belt, and quasi-linear between 3°S and 1°N, with wind anomalies of 0.15–0.4 m s^{-1} correlated with SST anomalies of 0.15–0.4 °C (Figure 8). The LN mechanism seems to be the strongest between 2°N and the Equator, and around 4.5°S, with SST gradients of 0.05–0.1 °C per latitude degree leading to 0.15–0.5 m s^{-1} (Figure 11). Surprisingly, and in spite of an obvious influence at the seasonal scale (the wind accelerations between the Equator and the coast seasonally coincide with the front intensification, see Figure 3), the northern edge of the front (around 1°N) seems to have a lesser impact on surface-wind fluctuations at intraseasonal time-scales around 3–4°N, with only 0.2 m s^{-1} responding to slightly less than 0.1 °C per latitude degree (Figure 11). Between the Equator and the coast, indeed, the wind fluctuations are also controlled by the LALC, which progressively settles between the Equator and the coast in MJ, and in which intraseasonal fluctuations partly fuel themselves with latent heat release at the coast, before being damped within 2–3 days (Leduc-Leballeur *et al.*, 2013).

In contrast, south of 1°N both re-analyses show that pressure gradients in the whole MABL (and even above) clearly respond to the SST gradients, in a way sufficient to explain the inversion of observed surface-wind anomalies within a week. This will in turn create a warm SST anomaly at the Equator within a few days, together with positive SST gradient anomalies, which will accelerate surface winds, etc., completing a cycle in about 2 weeks: this supports the hypothesis of an equatorial air–sea negative feedback sustaining a quasi-biweekly oscillation, and suggests that, in MJ, the whole regional low tropospheric circulation in the eastern tropical Atlantic is influenced by this oscillation. Eventually, the latter is the most pronounced in the equatorial belt (1°N to 1°S), where both mechanisms – SW and LN – combine to build the wind response at the Equator.

In short, in a highly sensitive region such as the eastern equatorial Atlantic – with a very intense SST front and weak Coriolis force – not only amplitudes but also the delay of the responses (oceanic as well as atmospheric) must be correct in order for a model to reproduce a realistic intraseasonal variability of low tropospheric winds. The SW and LN mechanisms are intrinsically linked, but this study suggests that their conceptual distinction, with different time- and space-lagged responses, could be very useful to work on the models parametrizations (especially planetary boundary and surface layers). Alternatively, Bryan *et al.* (2010) discussed the importance of activating the air–sea coupling in a global atmospheric model for obtaining a realistic correlation between the SST and the surface wind. They emphasized particularly the importance of the oceanic grid, which must be at least eddy-resolving, suggesting that a weak oceanic resolution was the first reason why global coupled models still tend to underestimate the strength of the atmospheric response to the SST (see also Colas *et al.*, 2012 for a similar discussion). Further investigations are therefore needed on these issues, with numerical coupled models of higher resolution.

Acknowledgements

We would like to thank Dr Justin Small and Dr Han Nguyen for their excellent review comments, which contributed to improve the article tremendously. This work benefited from a grant from Université Pierre et Marie Curie (Emergence 2010), and the Institut Pierre-Simon Laplace's server and data storage (Climserv).

References

Athie G, Marin F. 2009. Cross-equatorial structure and temporal modulation of intraseasonal variability at the surface of the tropical Atlantic Ocean. *J. Geophys. Res.* **113**: C08020, doi: 10.1029/2007JC004332.

Back LE, Bretherton CS. 2009. On the relationship between SST gradients, boundary layer winds, and convergence over the Tropical Oceans. *J. Clim.* **22**: 4182–4196.

Bourras D, Reverdin G, Giordani H, Caniaux G. 2004. Response of the atmospheric boundary layer to a mesoscale oceanic eddy in the northeast Atlantic. *J. Geophys. Res.* **109**: D18114, doi: 10.1029/2004JD004799.

Bryan F, Tomas R, Dennis JM, Chelton DB, Loeb NG, McClean JL. 2010. Frontal scale air–sea interaction in high-resolution coupled climate models. *J. Clim.* **23**: 6277–6291.

Caniaux G, Giordani H, Redelsperger J-L, Guichard F, Key E, Wade M. 2011. Couplings between the Atlantic cold tongue and the African monsoon in boreal spring and summer. *J. Geophys. Res.* **116**: C04003, doi: 10.1029/2010JC006570.

Chelton DB, Xie S-P. 2010. Coupled ocean–atmosphere interaction at oceanic mesoscales. *Oceanography* **23**: 52–69.

Chelton DB, Esbensen SK, Schlax MG, Thum N, Freilich MH, Wentz FJ, Gentemann CL, McPhaden MJ, Schopf PS. 2001. Observations of coupling between surface wind stress and sea surface temperature in the eastern tropical Pacific. *J. Clim.* **14**: 1479–1498.

Chelton DB, Schlax MG, Samelson RM, de Szoeke RA. 2007. Global observation of large oceanic eddies. *Geophys. Res. Lett.* **34**: L15606, doi: 10.1029/2007GL030812.

De Coëtlogon G, Janicot S, Lazar A. 2010. Intraseasonal variability of the ocean–atmosphere coupling in the Gulf of Guinea during boreal spring and summer. *Q. J. R. Meteorol. Soc.* **136**: 426–441.

Colas F, McWilliams JC, Capet X, Kurian J. 2012. Heat balance and eddies in the Peru–Chile current system. *Clim. Dyn.* **39**: 509–529.

Cook KH. 1999. Generation of the African Easterly Jet and its role in determining west African precipitation. *J. Clim.* **12**: 1165–1184.

Dee DP, Uppala SM, Simmons AJ, Berrisford P, Poli P, Kobayashi S, Andrae U, Balmaseda MA, Balsamo G, Bauer P, Bechtold P, Beljaars ACM, van de Berg L, Bidlot J, Bormann N, Delsol C, Dragani R, Fuentes M, Geer AJ, Haimberger L, Healy SB, Hersbach H, Hólm EV, Isaksen L, Kållberg P, Köhler M, Matricardi M, McNally AP, Monge-Sanz BM, Morcrette J-J, Park B-K, Peubey C, de Rosnay P, Tavolato C, Thépaut J-N, Vitart F. 2011. The ERA-Interim reanalysis: Configuration and performance of the data assimilation system. *Q. J. R. Meteorol. Soc.* **137**: 553–597.

Giordani H, Planton S. 2000. Modeling and analysis of ageostrophic circulation over the Azores oceanic front during the SEMAPHORE experiment. *Mon. Weather Rev.* **128**: 2270–2287.

Giordani H, Caniaux G. 2011. Diagnosing vertical motion in the equatorial Atlantic. *Ocean Dyn.* **1**: 233.

Giordani H, Caniaux G, Voldoire A. 2013. Intraseasonal mixed-layer heat budget in the equatorial Atlantic during the cold tongue development in 2006. *J. Geophys. Res.: Oceans* **118**: 1–22, doi: 10.1029/2012JC008280.

Giordani H, Planton S, Benech B, Kwon B-H. 1998. Atmospheric boundary layer response to sea surface temperatures during the SEMAPHORE experiment. *J. Geophys. Res.* **103**: 25,047–25,060, doi: 10.1029/98JC00892.

Hastenrath S. 1991. *Climate Dynamics of the Tropics.* Kluwer Academic Publishers: Dordrecht, The Netherlands.

Hayes SP, McPhaden MJ, Wallace JM. 1989. The influence of sea-surface temperature on surface wind in the eastern equatorial Pacific: Weekly to monthly variability. *J. Climate* **2**: 1500–1506.

Huffman GJ, Adler RF, Bolvin DT, Gu G, Nelkin EJ, Bowman KP, Hong Y, Stocker EF, Wolff DB. 2007. The TRMM Multisatellite Precipitation Analysis (TMPA): Quasi-global, multiyear, combined-sensor precipitation estimates at fine scales. *J. Hydrometeorol.* **8**: 38–55.

Jochum M, Manalotte-Rizzoli P, Busalacchi A. 2004. Tropical instability waves in the Atlantic Ocean. *Ocean Modell.* **7**: 145–163.

Jouanno J, Marin F, du Penhoat Y, Sheinbaum J, Molines J-M. 2011. Seasonal heat balance in the upper 100 m of the equatorial Atlantic Ocean. *J. Geophys. Res.* **116**: C09003, doi: 10.1029/2010JC006912.

Kikuchi K, Wang B. 2009. Global perspective of the Quasi-biweekly Oscillation. *J. Clim.* **22**: 1340–1359.

Knippertz P, Fink AH, Schuster R, Trentmann J, Schrage JM, Yorke C. 2011. Ultra-low clouds over the southern West African monsoon region. *Geophys. Res. Lett.* **38**: L21808, doi: 10.1029/2011GL049278.

Lafore J-P, Flamant C, Guichard F, Parker DJ, Bouniol D, Fink AH, Giraud V, Gosset M, Hall N, Höller H, Jones SC, Protat A, Roca R, Roux F, Saïd F. 2011. Progress in understanding of weather systems in West Africa. *Atmos. Sci. Lett.* **12**: 7–12.

Lavaysse C, Flamant C, Janicot S, Knippertz P. 2010. Links between African easterly waves, midlatitude circulation and intraseasonal pulsations of the West African heat low. *Q. J. R. Meteorol. Soc.* **136**: 141–158.

Leduc-Leballeur M, Eymard L, de Coëtlogon G. 2011. Observation of the marine atmospheric boundary layer in the Gulf of Guinea during the 2006 boreal spring. *Q. J. R. Meteorol. Soc.* **137**: 992–1003.

Leduc-Leballeur M, de Coëtlogon G, Eymard L. 2013. Air–sea interaction in the Gulf of Guinea at intraseasonal timescales: wind bursts and coastal precipitation in boreal spring. *Q. J. R. Meteorol. Soc.* **139**: 387–400, doi: 10.1002/qj.1981.

Lindzen RS, Nigam S. 1987. On the role of sea surface temperature gradients in forcing low-level winds and convergence in the tropics. *J. Atmos. Sci.* **44**: 2418–2436.

Liu WT, Xie X, Polito PS, Xie S-P, Hashizume H. 2000. Atmospheric manifestation of tropical instability wave observed by QuikSCAT and Tropical Rain Measuring Mission. *Geophys. Res. Lett.* **27**: 2545–2548.

Maloney ED, Chelton DB. 2006. An assessment of the SST influence on surface wind stress in numerical weather prediction and climate models. *J. Clim.* **19**: 2743–2762.

Marin F, Caniaux G, Bourlès B, Giordani H, Gouriou Y, Key E. 2009. Why were sea surface temperatures so different in the eastern equatorial Atlantic in June 2005and 2006? *J. Phys. Oceanogr*, **39**: 1416–1431.

Masson S, Terray P, Madec G, Luo J-J, Yamagata T, Takahashi K. 2012. Impact of intra-daily SST variability on ENSO characteristics in a coupled model. *Clim. Dyn.* **39**: 681–707, doi: 10.1007/s00382-011-1247-2.

Matsuno T. 1966. Quasi-geostrophic motions in the equatorial area. *J. Meteorol. Soc. Jpn.* **44**: 25–43.

Meynadier R, Bock O, Gervois S, Guichard F, Redelsperger J-L, Agustí-Panareda A, Beljaars A. 2010. West African monsoon water cycle: 2. Assessment of numerical weather prediction water budgets. *J. Geophys. Res. Atmos.* **115**: D19107.

Nguyen H, Duvel J-P. 2008. Synoptic wave perturbations and convective systems over equatorial Africa. *J. Clim.* **23**: 6372–6388.

Nguyen H, Thorncroft C, Zhang C. 2011. Guinean coastal rainfall of the West African monsoon. *Q. J. R. Meteorol. Soc.* **137**: 1828–1840.

O'Neill LW, Esbensen SK, Thum N, Samelson R, Chelton DB. 2010a. Dynamical analysis of the boundary layer and surface wind responses to mesoscale SST perturbations. *J. Clim.* **23**: 559–581.

O'Neill LW, Chelton DB, Esbensen SK. 2010b. The effects of SST-induced surface wind speed and direction gradients on midlatitude surface vorticity and divergence. *J. Clim.* **23**: 255–281.

Peter A-C, Le Hénaff M, du Penhoat Y, Menkes CE, Marin F, Vialard J, Caniaux G, Lazar A. 2006. A model study of the seasonal mixed layer heat budget in the equatorial Atlantic. *J. Geophys. Res.* **111**: C06014, doi:10.1029/2005JC003157.

Pu B, Cook KH. 2010. Dynamics of the West African westerly jet. *J. Climate* **23**: 6263–6276, doi: http://dx.doi.org/10.1175/2010JCLI3648.1.

Reynolds RW, Smith TM, Liu C, Chelton DB, Caset KS, Schlax MG. 2007. Daily high-resolution blended analyses for sea surface temperature. *J. Clim.* **20**: 5473–5496.

Saha S, Moorthi S, Pan H-L, Wu X, Wang J, Nadiga S, Tripp P, Kistler R, Woollen J, Behringer D, Liu H, Stokes D, Grumbine R, Gayno G, Wang J, Hou Y-T, Chuang H-Y, Juang H-MH, Sela J, Iredell M, Treadon R, Kleist D, Van Delst P, Keyser D, Derber J, Ek M, Meng J, Wei H, Yang R, Lord S, Van Den Dool H, Kumar A, Wang W, Long C, Chelliah M, Xue Y, Huang B, Schemm J-K, Ebisuzaki W, Lin R, Xie P, Chen M, Zhou S, Higgins W, Zou C-Z, Liu Q, Chen Y, Han Y, Cucurull L, Reynolds RW, Rutledge G, Goldberg M. 2010. The NCEP climate forecast system reanalysis. *Bull. Am. Meteorol. Soc.* **91**: 1015–1057.

Samelson RM, Skyllingstad ED, Chelton DB, Esbensen SK, O'Neill LW, Thum N. 2006. On the coupling of wind stress and sea surface temperature. *J. Clim.* **19**: 1557–1566.

Small JR, Xie S-P, Wang Y, Esbensen SK, Vickers D. 2005. Numerical simulation of boundary layer structure and cross-equatorial flow in the eastern Pacific. *J. Atmos. Sci.* **62**: 1812–1830.

Sobel AH, Maloney ED, Bellon G, Frierson DM. 2010. Surface fluxes and tropical intraseasonal variability: A reassessment. *J. Adv. Model. Earth Syst.* **2**: Art. #2, 27 pp.

Spall MA. 2007. Midlatitude wind stress-sea surface temperature coupling in the vicinity of oceanic fronts. *J. Clim.* **20**: 3785–3801.

Stevens B. 2002. Entrainment in stratocumulus mixed layers. *Quart. J. Roy. Meteor. Soc.* **128**: 2663–2690.

Sweet W, Fett R, Kerling J, La Violette P. 1981. Air–sea interaction effects in the lower troposphere across the north wall of the Gulf Stream. *Mon. Weather Rev.* **109**: 1042–1052.

Thorncroft CD, Nguyen H, Zhang C, Peyrille P. 2011. Annual cycle of the West African monsoon: Regional circulations and associated water vapour transport. *Q. J. R. Meteorol. Soc.* **137**: 129–147.

Trenberth KE, Stepaniak DP, Caron JM. 2000. The global monsoon as seen through the divergent atmospheric circulation. *J. Clim.* **13**: 3969–3993.

Wade M, Caniaux G, Du Penhoat Y. 2011. Variability of the mixed layer heat budget in the eastern equatorial Atlantic during 2005–2007 as inferred using Argo floats. *J. Geophys. Res.* **116**: C08006, doi: 10.1029/2010JC 006683.

Wallace JM, Mitchell TP, Deser C. 1989. The influence of sea-surface temperature on surface wind in the eastern equatorial Pacific: Seasonal and interannual variability. *J. Clim.* **2**: 1492–1499.

Weingartner TJ, Weisberg RH. 1991. On the annual cycle of equatorial upwelling in the central Atlantic Ocean. *J. Phys. Oceanogr.* **21**: 68–82.

Xie S-P. 2004. Satellite observations of cool ocean–atmosphere interaction. *Bull. Am. Meteorol. Soc.* **85**: 195–208.

Zhang C, Nolan DS, Thorncroft CD, Nguyen H. 2008. Shallow meridional circulations in the tropical atmosphere. *J. Clim.* **21**: 3453–3470.